PRECISE MUON DRIFT TUBE DETECTORS FOR HIGH BACKGROUND RATE CONDITIONS

vorgelegt von
Albert Engl
geboren in Tegernsee

München, den 1. Juli 2011

1. Gutachter: Prof. Dr. Otmar Biebel

2. Gutachter: Prof. Dr. Wolfgang Dünnweber

Tag der mündlichen Prüfung: 04.08.2011

Die Neugierde steht immer an erster Stelle eines Problems,
das gelöst werden will.
(Galileo Galilei)

ABSTRACT

The muon spectrometer of the ATLAS-experiment at the Large Hadron Collider consists of drift tube chambers, which provide the precise measurement of trajectories of traversing muons. In order to determine the momentum of the muons with high precision, the measurement of the position of the muon in a single tube has to be more accurate than $\sigma \leq 100$ μm.

The large cross section of proton-proton-collisions and the high luminosity of the accelerator cause relevant background of neutrons and γs in the muon spectrometer. During the next decade a luminosity upgrade [1] to $5 \cdot 10^{34} \text{cm}^{-2} \text{s}^{-1}$ is planned, which will increase the background counting rates considerably. In this context this work deals with the further development of the existing drift chamber technology to provide the required accuracy of the position measurement under high background conditions. Two approaches of improving the drift tube chambers are described:

- In regions of moderate background rates a faster and more linear drift gas can provide precise position measurement without changing the existing hardware.

- At very high background rates drift tube chambers consisting of tubes with a diameter of 15 mm are a valuable candidate to substitute the CSC muon chambers.

The single tube resolution of the gas mixture $\text{Ar} : \text{CO}_2 : \text{N}_2$ in the ratio of $96 : 3 : 1$ Vol %, which is more linear and faster as the currently used drift gas $\text{Ar} : \text{CO}_2$ in the ratio of $97 : 3$ Vol %, was determined at the Cosmic Ray Measurement Facility at Garching and at high γ-background counting rates at the Gamma Irradiation Facility at CERN. The alternative gas mixture shows similar resolution without background. At high background counting rates it shows better resolution as the standard gas. To analyse the data the various parts of the setup have to be aligned precisely to each other. The change to an alternative gas mixture allows the use of the existing hardware.

The second approach are drift tubes with halved radius, which also provide better high rate capability. The single tube resolution of these 15 mm drift tubes was determined to be 95 μm at the H8 test facility at CERN using a muon beam with an energy of 140 GeV.

ZUSAMMENFASSUNG

Das Myonspektrometer des ATLAS-Experiments am Large Hadron Collider besteht aus Kammern von Hochdruckdriftrohren, die die Trajektorien der Myonen vermessen. Damit der Impuls der Myonen aus der Krümmung der Spur mit hoher Genauigkeit gemessen werden kann, muss der Ort des Myondurchgangs in einem einzelnen Driftrohr mit einer Genauigkeit von $\sigma \leq 100 \ \mu$m gemessen werden.

Der große Wirkungsquerschnitt für Proton-Proton-Kollisionen und die hohe Luminosität des Beschleunigers verursachen bedeutenden Untergrund an Neutronen und Photonen im Myonspektrometer. In der nächsten Dekade ist geplant, die Luminosität auf $5 \cdot 10^{34} \mathrm{cm}^{-2} \mathrm{s}^{-1}$ zu erhöhen [1], was mindestens im selben Maße die Untergrundzählrate erhöhen wird. Die vorliegende Arbeit beschäftigt sich in diesem Zusammenhang mit der Weiterentwicklung der bestehenden Driftrohrkammertechnologie, um auch bei hohem Untergrund die geforderte Genauigkeit der Ortsmessung zu gewährleisten. Es werden zwei Ansätze für die Verbesserung der Driftrohrkammern beschrieben:

- In Regionen mittelmäßiger Untergrundzählraten kann ein schnelleres und lineareres Driftgas weiterhin die präzise Ortsmessung gewährleisten ohne die vorhandene Hardware auszutauschen.

- Bei sehr hohen Untergrundraten liefern Driftrohrkammern, bestehend aus Rohren mit einem Durchmesser von 15 mm, die geforderte Ortsauflösung. Diese können die CSC Myon-Kammern ersetzen.

Das Ortsauflösungsvermögen des Gasgemisches $\mathrm{Ar} : \mathrm{CO}_2 : \mathrm{N}_2$ im Verhältnis $96 : 3 : 1$ Vol %, welches linearer und schneller ist als das bisher verwendete Gemisch aus $\mathrm{Ar} : \mathrm{CO}_2$ im Verhältnis $97 : 3$ Vol %, wurde am Höhenstrahlungsmessstand in Garching sowie in der Gamma Irradiation Facility am CERN auch bei hohen γ-Untergrundzählraten gemessen. Das neue Gasgemisch besitzt vergleichbare Ortsauflösung ohne Untergrund. Bei hohen Untergrundzählraten weist es aber ein deutlich besseres Auflösungsvermögen gegenüber dem Standardgas auf. Für die Auswertung der Messdaten wurden die verschiedenen Bestandteile des Messaufbaus präzise zueinander ausgerichtet.

Durch die Verwendung von Driftrohren mit halbiertem Rohrradius erreicht man eine deutlich bessere Hochratenfestigkeit. Das Ortsauflösungsvermögen dieser 15 mm Driftrohre wurde am CERN in der H8 Messhalle mit einem 140 GeV Myonstrahl zu 95 μm bestimmt.

CONTENT

1 LHC AND THE ATLAS DETECTOR

1.1 LHC

To understand matter and the fundamental interactions, high energetic particles are collided. At the European laboratory for particle physics CERN near Geneva one of the largest particle accelerators the Large Hadron Collider LHC [2] is located. The LHC ring has a circumference of about 27 km and is designed for a center of mass energy of 14 TeV for proton collisions. For proton acceleration the energy losses due to synchrotron radiation, which are proportional to the fourth power of E/m, are far smaller than for electrons.

The layout of the LHC and the stages used for particle injection and pre-acceleration are shown in fig. 1.1. Free protons are produced by ionizing hydrogen atoms, which are accelerated in a LINAC to an energy of 50 MeV. After passing the booster and the proton synchrotron PS the protons are fed with an energy of 25 GeV into the super proton synchrotron SPS. This is a storage ring with an circumference of about 6 km, which brings the protons up to an energy of 450 GeV. After injection into the LHC ring the protons are accelerated to the nominal beam energy of 7 TeV. To keep the particles on their circular orbit super-conducting dipoles are used producing a magnetic field of around 8 T. The two proton beams are moving in opposite direction in separated beam pipes and are brought to collision at 4 interaction points where the experiments are situated.

The design luminosity of the LHC is 10^{34} cm^{-2} s^{-1} and the spacing between consecutive clustered proton bunches in each beam is 25 ns, corresponding to a frequency of collinding bunches at the interaction points of 40 MHz.

There are 4 main experiments at LHC. ATLAS [3] and CMS [4] are multi purpose detectors to cover a wide range of physics processes (e.g. search for Higgs or SUSY particles). The dedicated experiment for the detailed investigation of B-mesons is LHCb [5]. The LHC can also be operated with heavy ions (e.g. Pb). Therefore the detector ALICE (A Large Ion Collider Experiment) [6] is in place.
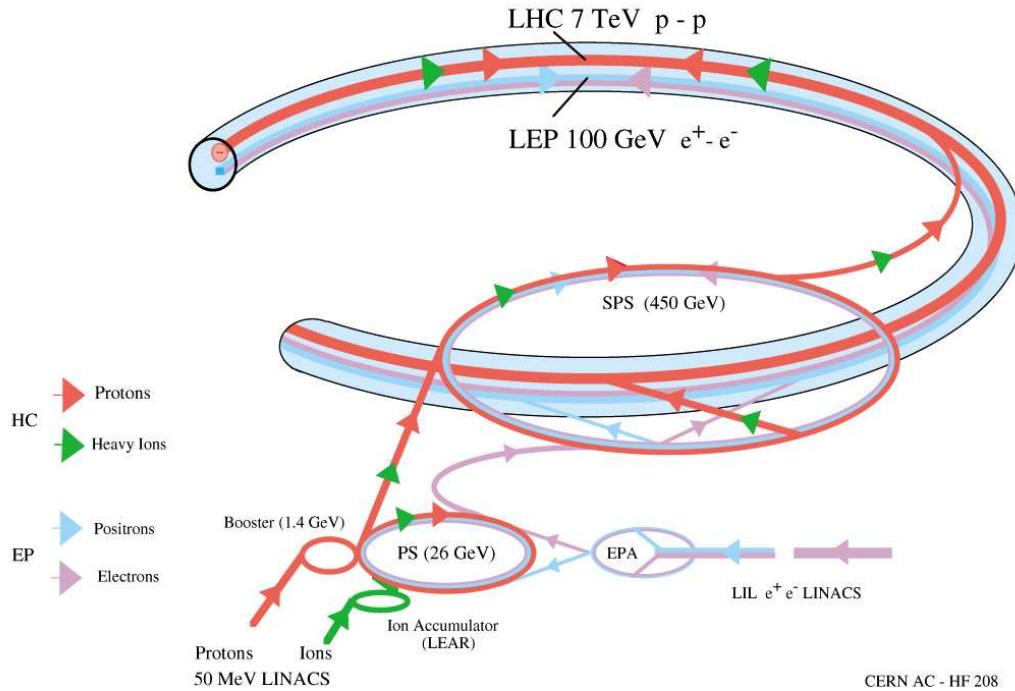
The LHC injection complex

Figure 1.1: Schematic layout of the Large Hadron Collider. [7]

1.2   The ATLAS Detector

The ATLAS (A Toroidal LHC Apparatus) detector is built in layers around the particle collision point. It has a cylindric shape with a length of 44 m and a diameter of 25 m and weighs about 7000 t (fig. 1.2). The central part commonly known as 'barrel' is arranged concentrically around the beam axis of LHC. The outer circular sections are called 'endcaps'. Starting at the interaction point, the barrel as well as the endcaps of ATLAS consist of the Inner Detector, the Electromagnetic and Hadronic Calorimeter and the huge Muon Spectrometer.

1.2.1   *Inner Detector*

Closest to the beam pipe is located the Inner Detector [9], shown in fig. 1.3. It is responsible for a precise track reconstruction, the momentum measurement as well as for the vertex reconstruction. The components, starting with the innermost, are the Silicon Pixel Detector (SPD), the Semiconductor Tracker (SCT) and the Transition Radiation Tracker (TRT). The SPD has a position resolution
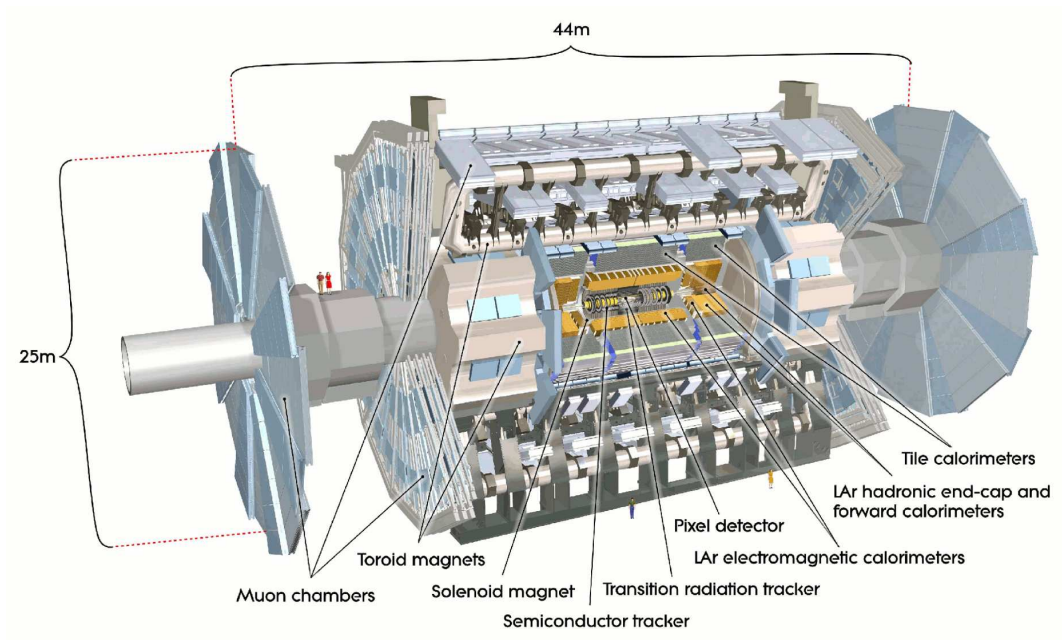
Figure 1.2: Cut-away view of the ATLAS detector. [8]

of 60 μm in beam direction and 12 μm perpendicular to it and is arranged in three layers. This system is surrounded by the SCT, which consists of 4 barrel layers and 9 endcap layers of silicon strip detectors. The TRT system completes the Inner Detector and provides up to 36 points for each particle trajectory and further allows the separation of electrons and pions. The whole Inner Detetcor is embedded in a strong solenoidal magnetic field.
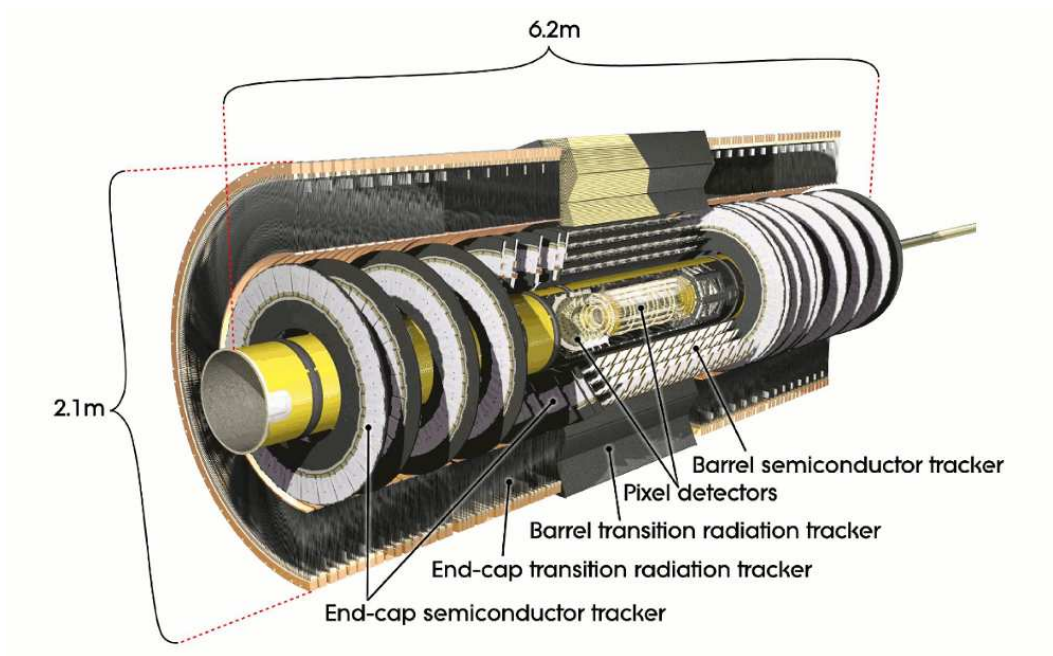
Figure 1.3: Cut-away view of the ATLAS inner detector. [8]

1.2.2 *Calorimeter*

The calorimeter system (fig. 1.4) [10] is surrounding the Inner Detector. The inner part, the electromagnetic calorimeter (ECAL), is measuring the energy of electromagnetic showers produced by electrons, positrons and photons. The ECAL consists of accordion-shaped lead absorber plates and the space inbetween is filled with liquid argon. Finely segmented electrodes collect the deposited charge of passing particles and it is possible to precisely measure the shower shape. The
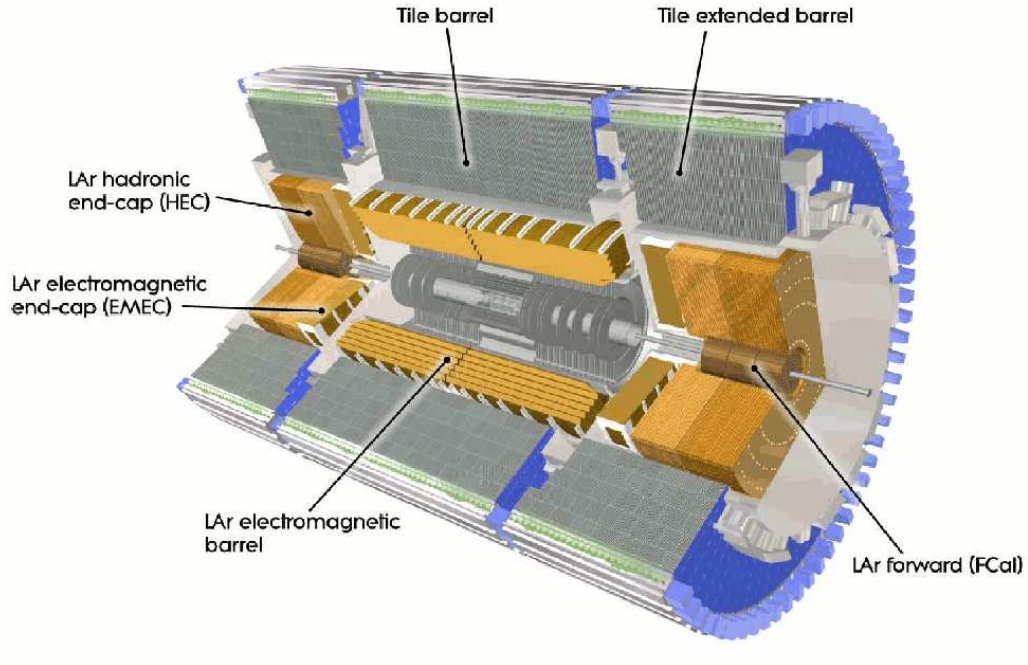

Figure 1.4: Cut-away view of the ATLAS calorimeter. [8]

outer part, the hadronic calorimeter (HCAL), performs the energy measurement of charged and neutral hadrons. The HCAL is a system of iron absorbers and scintillating tiles in the barrel region, whereas in the endcaps a liquid argon sampling calorimeter with copper absorber is used. The design energy resolution is $(10\%/\sqrt{E} \oplus 1\%)$ for the ECAL and $(50\%/\sqrt{E} \oplus 3\%)$ for the HCAL [10].

1.2.3 *Muon Spectrometer*

The largest part of the ATLAS detector is covered by the muon spectrometer [11], forming the outer shell of the experiment. Two different types of detectors are used. Trigger chambers are providing fast information on timing and rough position information for throughgoing muons and tracking chambers provide precisely reconstructed muon trajectories. Due to the presence of the toroidal magnetic field muon tracks are curved and the muon momentum can be determined via $p = R \cdot q \cdot B$, where R is the track radius, q the muon charge and B the B-field.
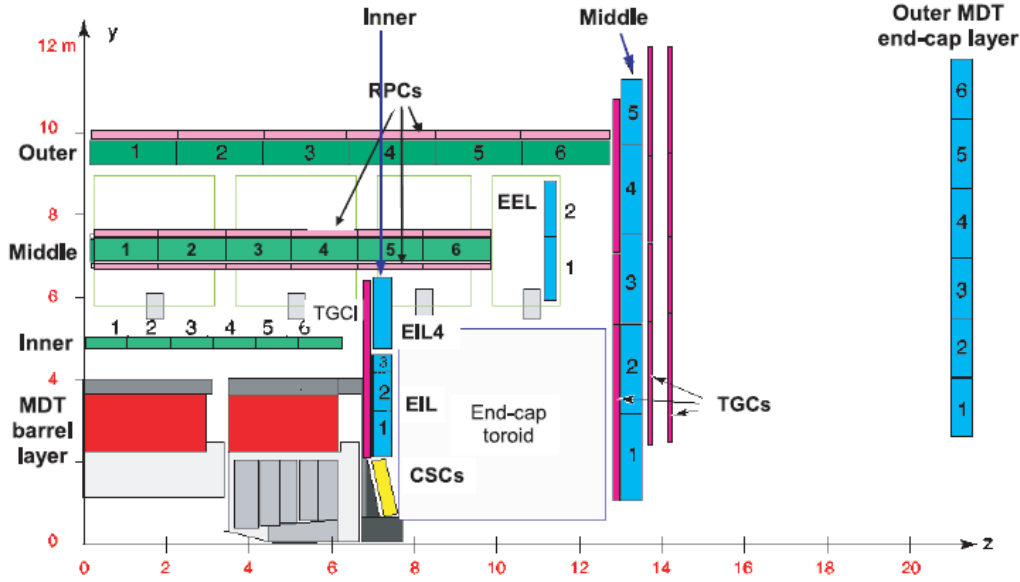

Figure 1.5: Cross-section showing a quarter of the muon spectrometer in a plane containing the beam axis. [8]

Fig. 1.5 shows a cross section of the muon spectrometer. In the barrel region the rectangular muon chambers are arranged in three concentric cylinders (Inner, Middle and Outer) around the beam axis. Whereas in the endcaps the trapezoidal-shaped chambers form discs. In the endcap region nearest to the beam pipe cathode strip chambers (CSC) are used, which provide higher rate capability. The precise track reconstruction is performed by monitored drift tube (MDT) chambers (see chapter 2) and as trigger resistive plate chambers (RPC) are used in the barrel region and thin gap chambers (TGC) in the endcap regions.

The design goal of the ATLAS muon spectrometer is a transverse momentum resolution of

Eqn. 1.1:
$$\frac{\Delta p}{p} = 10\%$$

for a momentum of 1 TeV. This translates into a single tube resolution of about 80 μm [11].

2   MUON CHAMBER

This chapter describes the principle of drift tube chambers [12, 13, 14, 15], the readout electronics and the performance under normal and high rate conditions.

2.1   Principle of Drift Tubes

In the ATLAS muon spectrometer drift tubes of 30 mm diameter and a wall thickness of 400 μm are used. The length of the tubes differs from 1 m to 6 m depending on the position in the muonspectrometer. The tubes are filled with an Argon and CO_2 gas mixture of (93:7 vol%) at an absolute pressure of 3 bar. The voltage at the gold plated W-Re anode wire (diameter 50 μm) is 3080 V.
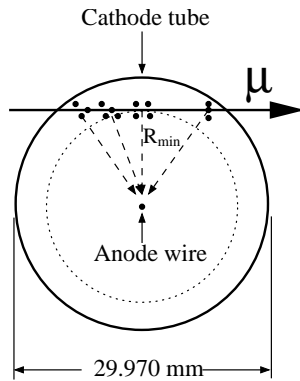

Figure 2.1: The principle of a drift tube. [8]

An ionising particle creates on its path through the drift gas electron-ion pairs. In the radially symmetric electrical field

Eqn. 2.1:
$$E(r) = \frac{U}{ln\frac{b}{a}} \cdot \frac{1}{r},$$

where U is the anode wire potential, b the tube and a the wire radius, the primary electrons drift towards the wire (fig. 2.1). Near the wire the drift field exceeds the critical field strength for secondary ionization and a gas avalanche develops.

Due to the gas gain of 20000, the signal on the wire reaches a level to be measureable. The time difference between the appearance of this signal and the pass of the ionising particle through the tube, given by the trigger chambers, defines the drift time. If the particle passes the gas volume near the tube wall, the drift time is about 700 ns. As described in chapter 4 the drift radius can be derived from the measured drift time. To reach a spatial resolution of about 50 μm per chamber, the drift radius in a single tube has to be measured with a precision of better than 100 μm.

The upgrade of the muon drift tube chambers at increasing radiation rates at high-luminosity-LHC is the topic of this present work.

2.2 Assembly of a Drift Tube Chamber

To be able to reconstruct muon tracks, multiple drift tubes are assembled to a drift tube chamber, shown in fig. 2.2. The MDT chambers consist of 2 multilayers with 3 or 4 layers of drift tubes. These multilayers are glued on a support structure, which consists of two longitudinal (parallel to the anode wires) and three cross bars.

The wire is centered in each tube to a precision of 20 μm. In order to monitor geometrical deformations of a chamber [16], an optical alignment system is included in the support structure (RasNik) [17].

2.3 Readout Electronics of the Drift Tube Chamber

To enable electric services (see fig. 2.3), hedgehog boards are used. These boards are plugged on the endcaps and the grounding pins of the tubes. For noise reduction it is essential that each tube is equipped with a grounding pin. The high voltage (HV) hedgehog board connects the HV power line by a 1 MΩ current limiting resistor to the anode wire. It terminates the tube with its transmission line impedance of 383 Ω to suppress signal reflection at the open end of the wire. It also contains voltage stabilizing capacitors. The signal hedgehog board connects the tube to the mezzanine board, which contains the active readout electronics and decouples the HV by a 470 pF capacitor. The 10 kΩ resistor provides coupling
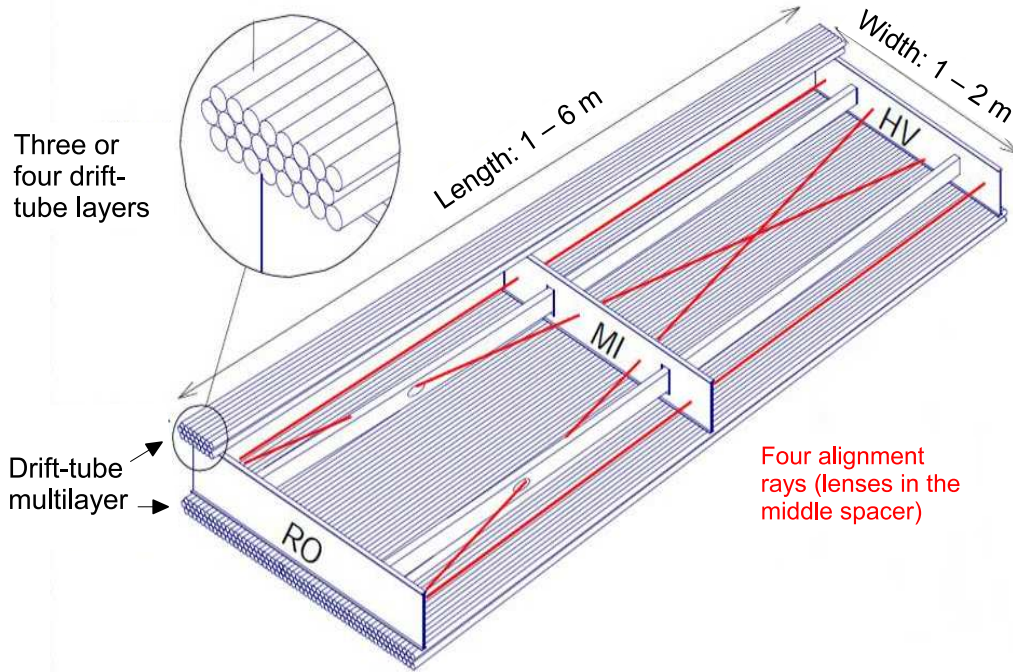
Figure 2.2: Mechanical structure of a MDT chamber. An aluminium space frame carrys two multi-layers of three or four drift tube layers. The optical alignment rays allow for monitoring of the internal geometry of the chamber. [8]

of the signal line to ground potential.

The mezzanine board contains the Time to Digital Converter (AMT [18]) chip and three Amplifier/Shaper/Discriminator (ASD [19]) chips. It is the basic readout element of the MDT chambers.

The raw signals from the tubes are routed via the signal hedgehog board to the mezzanine boards where they are amplified, shaped and discriminated by the ASD chips. The signals output of the ASDs are then routed to the AMT chip, where the times of leading and trailing edges are digitized. The measured times, including the information of the corresponding tube channel, are sent to the Chamber Service Module (CSM). The time is measured in units of the bunch crossing frequency (40 MHz) of the LHC machine. In the TDC the bunch crossing interval of 25 ns is subdivided by 32 via a Delay Locked Loop (DLL). Therefore the unit of time measurement is 25/32 ns.

The CSM collects the data of one muon chamber (up to 18 mezzanine boards) and routes this data via an optical fibre to the MDT Readout Driver (MROD),
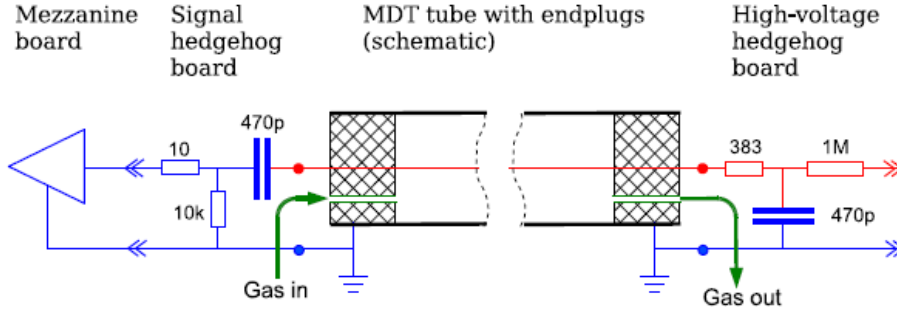
Figure 2.3: Service connections to a MDT tube. [20]

which then routes the combined data stream of several MDT chambers finally to the read out system. The CSM further distributes the control and trigger signals of the Trigger Timing Control (TTC) system, which receives the bunch crossing frequency of the LHC and the trigger signal of the trigger chamber system, to the mezzanine boards.

2.4 Performance at High Rate Conditions

2.4.1 Background Hit Rates at ATLAS

LHC plans to increase luminosity steadily from $1.2 \cdot 10^{33} \frac{1}{\text{cm}^2\text{s}}$ to $5 \cdot 10^{34} \frac{1}{\text{cm}^2\text{s}}$ in the next decade. So the MDT chambers will have to cope with higher background counting rates. Slow and fast neutrons as well as secondary γ's are the main sources of background, whilst charged hadrons, electrons and γ's will not pass the calorimeters.

Simulation results of the background rates at the nominal design luminosity of $10^{34} \frac{1}{\text{cm}^2\text{s}}$ in the different detector regions are shown in fig. 2.4 [21], where a quadrant of the ATLAS detector is displayed.
To account for uncertanties in the simulation a saftey factor of 5 has been included in the results. This factor contains uncertanties in the particle production cross section, in the conversion probability of neutrons and γ's in the tube walls and the gas as well as in the particle transport through the detector and dead material.

Including the safety factor, the expected counting rates in the barrel region (MDT
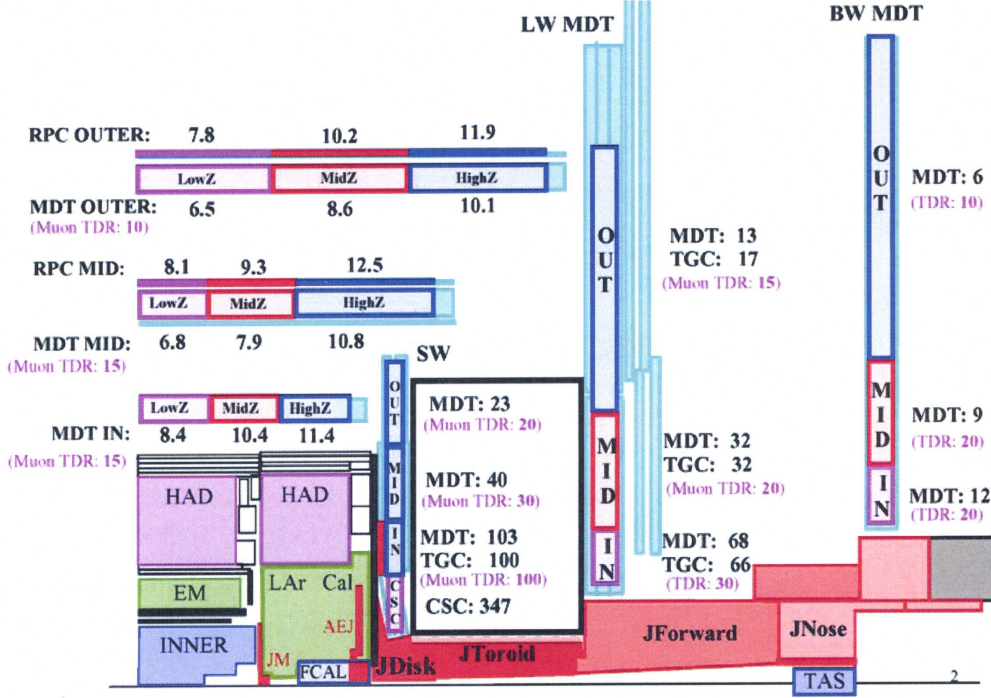
Figure 2.4: Expected simulated background hit rates in Hz/cm² at ATLAS without safety factor. [21]

In, Mid, Outer) and the big wheel (BW) of the muon spectrometer are in the range of 30 to 60 $\frac{\text{Hz}}{\text{cm}^2}$. In the rest of the endcap, especially close to the beam pipe the counting rates are partially ten times higher. The counting rates in the large wheel (LW) rise from 65 to 340 $\frac{\text{Hz}}{\text{cm}^2}$ and the small wheel (SW) expects rates between 150 and 500 $\frac{\text{Hz}}{\text{cm}^2}$ for the MDTs. In the innermost sector of the small wheels the CSCs have to cope with rates of 1700 $\frac{\text{Hz}}{\text{cm}^2}$.

Background measurements with the ATLAS detector were performed at a luminosity of $1.5 \cdot 10^{32} \frac{1}{\text{cm}^2\text{s}}$ and extrapolated to the design luminosity of $10^{34} \frac{1}{\text{cm}^2\text{s}}$ [22]. These data show, that the background hit rates are 2 - 10 $\frac{\text{Hz}}{\text{cm}^2}$ for the barrel region and the big wheel and 4 - 30 $\frac{\text{Hz}}{\text{cm}^2}$ for the large wheel. Regarding the small wheel counting rates in the range between 45 and 120 $\frac{\text{Hz}}{\text{cm}^2}$ were determined. These results are in agreement with the simulation without safety factor.

After the luminositiy upgrade all rates will be 5 times higher.

2.4.2 *Space Charge Effects*

As γs and neutrons are also ionising the drift gas, their signal superimpose the muon signal and particularly produce space charges. The influence of space charges on the performance of a drift tube with the present ATLAS gas mixture are described in the following [23, 24, 25, 26]. The ions created in the avalanche at the wire drift to the tube wall. Assuming that the ion mobility is constant and its value is $\mu = 0.52 \ \frac{cm^2}{Vs}$ and the drift velocity is given by

$$Eqn.\ 2.2: \qquad\qquad v = \mu \cdot E(r),$$

one can derive the drift time ions need to get from the anode wire to the tube wall as:

$$Eqn.\ 2.3: \qquad\qquad t = \int \frac{dx}{v} = \int \frac{dx}{\mu E(r)} = \frac{ln\frac{b}{a}}{\mu U} \int_a^b \frac{dr}{1/r}.$$

The integration leads to the following expression for the maximal ion drift time:

$$Eqn.\ 2.4: \qquad\qquad t_{max}^{ion} = \frac{ln\frac{b}{a}}{2U\mu}(b^2 - a^2),$$

where b is the tube radius of 15 mm, a the wire radius of 25 μm and $U = 3080$ V is the anode voltage. This leads to $t_{max}^{ion} = 4.23$ ms being the time scale ions need to reach the tube wall. Using tubes with half $= 7.5$ mm radius leads to $t_{max}^{ion} = 1.13$ ms $\approx \frac{1}{4}t_{max}^{ion}(15mm)$.

These ions modify the electric field for subsequent events. The field is lowered between anode wire and ion cloud and raised between ion cloud and tube wall. In case of a non-linear drift gas the drift velocity depends on the electric field and space charge effects will account in a resolution deterioration. Close to the

wire the decreased electric field leads to a reduced electron multiplication. Therefore the gas gain is lower (gain drop) and the signals are scaled down. Since the discriminator threshold remains fixed, the threshold crossing is shifted and the resolution deteriorates.
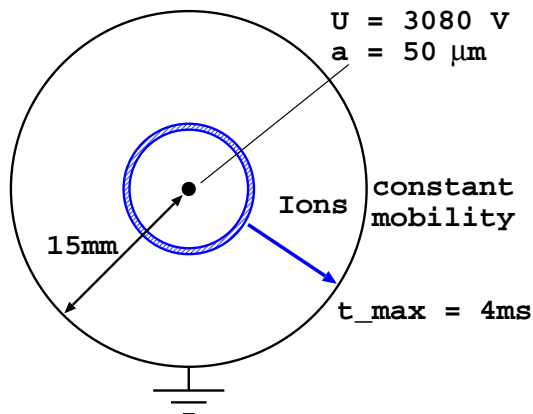

Figure 2.5: Drift tube with space charges.

According to [23, 24] the density of space charge (a schematic view is given in fig. 2.5) is given by

Eqn. 2.5:
$$\rho(r) = \frac{N_c G Q}{2\pi r \mu E(r)},$$

where N_c is the count rate per unit wire length along the tube, Q is the average charge deposit per background event, G is the gas gain and μ is the ion mobility. Using Gauss' theorem leads to the following expression:

Eqn. 2.6:
$$2\pi r E(r) = \frac{\gamma}{\epsilon_0} + \frac{1}{\epsilon_0} \int_a^r 2\pi r' \rho(r')\, dr',$$

with γ being the line charge (eqn. 2.9) on the anode wire. Differentiating both sides yields the differential equation

Eqn. 2.7: $\qquad E(r)^2 + r \cdot E(r) \cdot \dfrac{dE(r)}{dr} = c \qquad with \qquad c = \dfrac{N_c G Q}{2\pi \mu \epsilon_0}$

for the changed electric field. The solution of eqn. 2.7 is

Eqn. 2.8: $\qquad\qquad\qquad\qquad E(r) = \sqrt{c} \dfrac{k}{r} \sqrt{1 + \dfrac{r^2}{k^2}};$

where the parameter k is defined by the boundary condition $\int_a^b E(r)dr = U$. So the electric field depends on k and c and therefore on the background count rate N_c. Fig. 2.6 shows the shape of both parameters versus the couting rate. While k is decreasing with increasing rate, $\sqrt{c}$ is increasing. The gas gain G is depending on the line charge on the wire γ:

Eqn. 2.9: $\qquad\qquad\qquad\qquad \gamma = 2\pi\epsilon_0 a E(a).$

Using Diethorn's formula [27], G can be calculated:

Eqn. 2.10: $\qquad G = \left[\dfrac{\gamma}{2\pi\epsilon_0 a E_{min}(\rho_0)\frac{\rho_{gas}}{\rho_0}} \right]^{\frac{\gamma ln2}{2\pi\epsilon_0 \Delta V}} = \left[\dfrac{E(a)}{E_{min}(\rho_0)\frac{\rho_{gas}}{\rho_0}} \right]^{\frac{aE(a)ln2}{\Delta V}};$

$E_{min}(\rho_0)$ and ΔV are gas dependent parameters and are taken from earlier measurements. $E_{min}(1bar) = 24$ kV/cm [28] is the minimal electric field necessary for secondary ionisation, $E(a)$ is the space charge dependent electric field at the wire, $\Delta V = 34$ V [28] is the average ionisation potential of the gas mixture and ρ_{gas} and ρ_0 are gas densities.

Iterating eqns 2.7 - 2.10, due to the fact that different gain produces different space charge, one can calculate the electric field and the gas gain as a function of the background rate. The charge dependent parameters k and $\sqrt{c}$ are shown in fig. 2.6 for the 30 mm and 15 mm tube geometry.
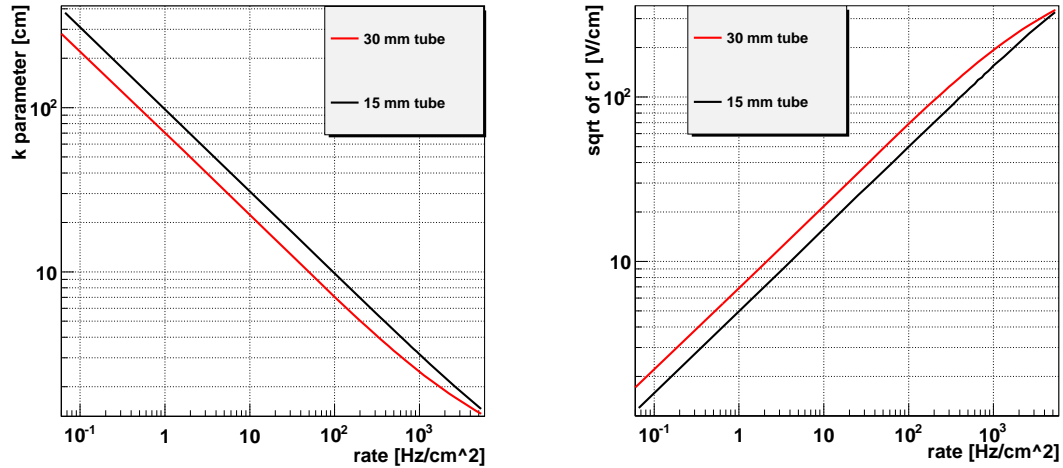

Figure 2.6: left: k parameter versus rate; right: square root of c versus rate. The rate is given in Hz/cm^2 and the parameters are plotted for 30 mm and 15 mm tubes.

The relative change of the electric field at a γ rate of 1400 $\frac{\text{Hz}}{\text{cm}^2}$, corresponding to high-luminosity-LHC conditions, and the gain drop as function of the rate is shown in fig. 2.7. The field changes up to 16 % for big radii of the 30 mm tubes. Hence the electrons drift velocity is higher and the rt relation changes significantly. Fluctuations of the space charges with time are then leading to a declined radius measurement. The gas gain is reduced by 30 % for 30 mm tubes and a counting rate of 1400 $\frac{Hz}{cm^2}$, whereas 15 mm tubes are less affected.

This effect and the gain drop are responsible for the measured resolution deterioration of the 30 mm drift tubes shown in fig. 2.8. One can see in black the resolution without background. It is about 200 μm for small radii and 60 μm for big radii. Due to γ-background rates of 1900 $\frac{\text{Hz}}{\text{cm}^2}$ the resolution deteriorates. For small radii the gain drop and for big radii field fluctuations account for the degradation.
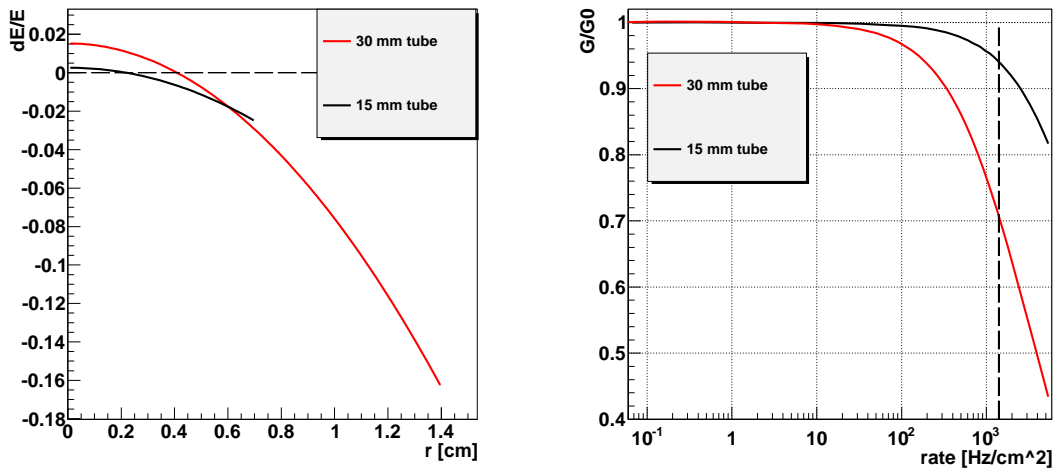
Figure 2.7: left: Change of the electric field for 1400 $\frac{\gamma}{cm^2 s}$. The E-field is on average reduced by 1.5 % (30 mm tube) and only 0.3 % for the 15 mm tubes at $r = 0$. At the tube wall, the E-fields are increased by 16 % (30 mm tubes) and 2.5 % (15 mm tubes). right: Gaindrop as function of background rate. The dashed line corresponds to 1400 $\frac{\gamma}{cm^2 s}$.
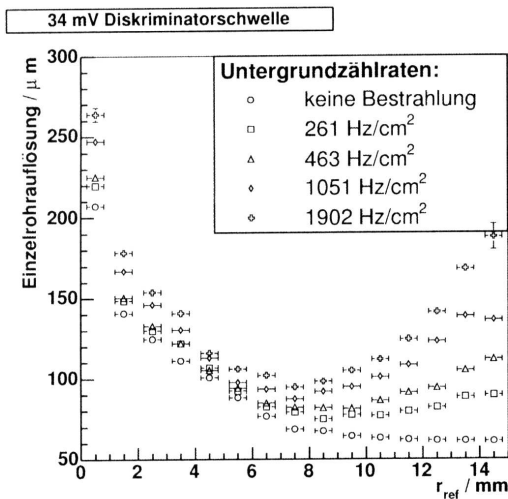

Figure 2.8: Single tube resolution measured with 30 mm drift-tubes versus radius with and without 662 keV γ background at the X5 test area at CERN. [29]

2.5   Solutions

Drift gases with electron drift velocities independent on the electric field strength are called linear drift gases. These gases are supposed to be independent on space charge fluctuations due to electric field changes. The gain drop effect close to the anode wire remain.

For detector regions with moderate background counting rates, as the barrel and the outer parts of the endcap wheels, an alternative drift gas can be a good possibility to achieve less resolution degradation. In this context a drift gas has to be faster to reduce the dead time of the tubes, and more linear to achieve less sensitivity to space charge fluctuations. Studies and results are presented in chapter 5.

MDT's consisting of 15 mm drift tubes (half of the present radius) can fulfill the requirements of the muon spectrometer at very high background counting rates. The gain drop (fig. 2.7, right) is reduced compared to 30 mm tubes and the change of the electric field (fig. 2.7, left) stays in the percent range leading to almost no shortening of the drift time spectrum and hence to almost no space charge fluctuations. Full details are given in chapter 6.

3 EXPERIMENTAL SETUPS

This chapter describes the three experimental setups, which were used for this thesis.

3.1 Cosmic Ray Measurement Facility

The CRMF (Cosmic Ray Measurement Facility) [30] is located in Garching (near Munich). A schematic cross section of the setup is shown in fig. 3.1. It consists of three ATLAS MDT muon chambers. The upper and the lower chamber are called reference chambers. The geometry, especially the wire positions, were determined using a x-ray tomograph [31]. These two chambers are used to provide precise muon tracks in order to analyse and compare data taken with the chamber in the middle, the test chamber.

To trigger on cosmic rays 3 layers of scintillation counters are included into the setup. One is located above the upper reference chamber, the other two below a 34.5 cm iron absorber. The coincidence of the three scintillation layers provides the start signal for the readout system. Due to the double-layer of the lower hodoscope with photomultiplier readout on opposite sides the time resolution of the trigger is 1 ns. The steel is used to harden the selected muon spectrum. Triggering muons have a minimal energy of about 600 MeV.

The two reference chambers were operated with the standard gas mixture $Ar:CO_2$ in the ratio of 93:7 Vol % at an absolute pressure of 3 bar, in a climatized room at 20 °C and the voltage on the anode wire was 3080 V. The test chamber was filled with the alternative gas mixtures containing partially N_2.
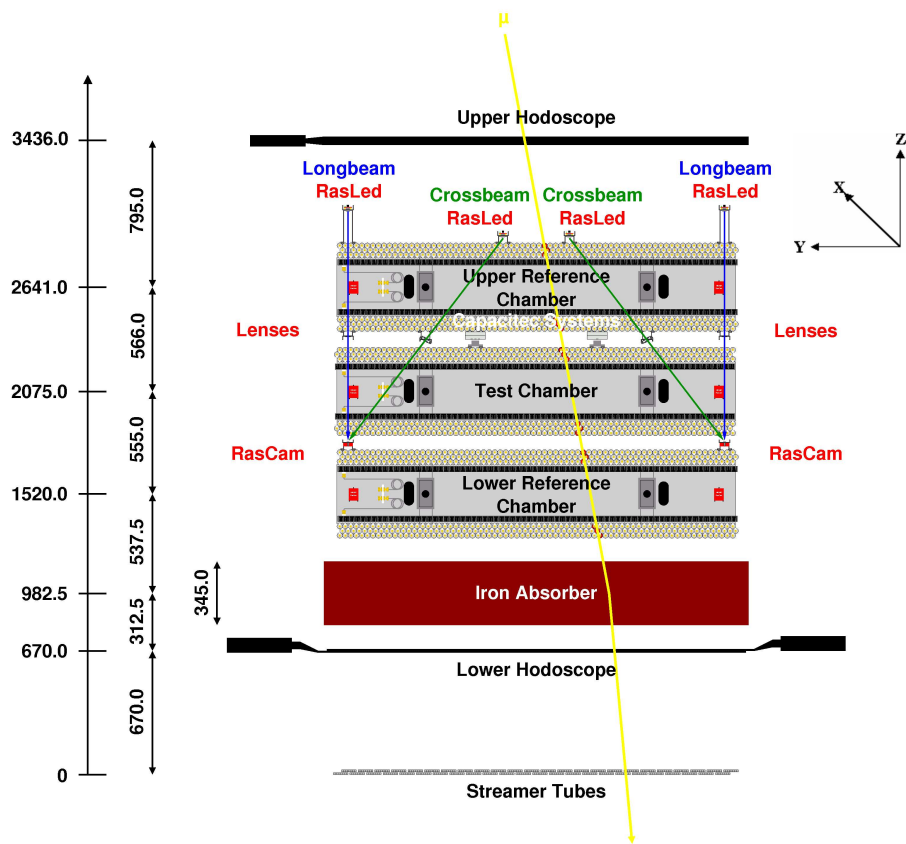
Figure 3.1: Schematic side view of the CRMF in Garching (Munich).

3.2 Gamma Irradiation Facility

The Gamma Irradation Facility (GIF) is located at CERN. In fig. 3.2 the setup is shown schematically. It is possible to irradiate muon chambers with high γ-background rates. The activity of the Cs137-source was 560 GBq (2009) enabling in a distance of 90 cm a γ flux density of up to a few thousand $\frac{Hz}{cm^2}$.

The setup consists of two muon chambers with 48 drift tubes, assembled in two multilayers with 3 tube layers each. Each tube has a diameter of 30 mm and is 50 cm long. The distance between the multilayers differed for the two chambers. It was 32 cm for the upper chamber and 9 cm for the lower one. Between the two chambers, 6 drift tubes with half the diameter, 15 mm, and a length of 1 m were located. The chambers were operated at standard ATLAS conditions. For the 15 mm tubes the high voltage at the wire was reduced to 2730 V in order to have the same electric drift field and gas gain as for the 30 mm tubes.

To trigger on cosmic muons a segmented hodoscope with four layers of scintillation counters was designed [37]. The counters of layer 1 and 3 (7 per layer) were parallel to the anode wires and their width was 40 mm. So one counter covers approximately one tube and therefore we get a raw muon road, defined by the hits in each of the two layers. In layer 2 and 4 the counters (5 per layer) were perpendicular to the wires with a width of 90 mm. These two layers enable a raw information of the muon track along the wire. The 4-fold coincidence of the layers defined the start signal for the readout system.

Since background influences the track reconstruction, the topmost and lowermost multilayer was shielded with lead bricks against γ-irradiation. Furthermore 15 cm of lead, located between the lower reference chamber and the lower hodoscope, hardened the selected muon spectrum.

Besides the determination of the high rate behaviour of the 15 mm tubes, a second issue of this test period was the determination of the single tube resolution under γ-background using the alternative gas mixture $Ar:CO_2:N_2 = 96:3:1$, which was filled into the unshielded lower multilayer of the upper reference chamber.
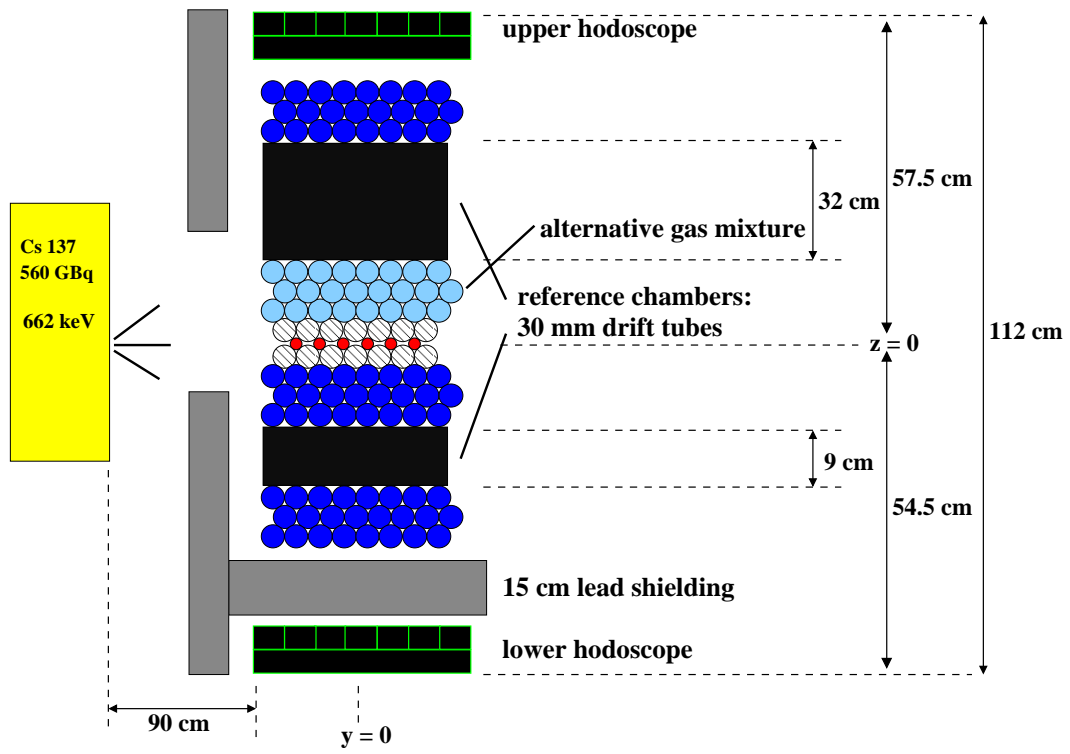
Figure 3.2: Schematic view of the setup in the Gamma Irradiation Facility at CERN.

3.3   Muon Beam at H8

To determine the single tube resolution of 15 mm tubes with high energy muons, measurements at the H8 [32, 33] facility at CERN were performed. The muon beam had an energy of 140 ± 40 GeV.

The track reference for this measurement should be provided by a silicon telescope, but unfortunately this system didn't work properly. So the 30 mm muon chambers from the GIF setup were used to provide the reference tracks. Fig. 3.3 shows the setup, where a bundle of 96 tubes with 15 mm diameter and 1.2 m length was tested.

The beam muon trigger was set up as the coincidence of two scintillation counters with a surface of 5×5 cm^2, slightly smaller than the available beam profile. Therefore only a small part of the chamber was irradiated.

We will see later in the data analysis that the muon beam was mostly parallel. ATLAS standard parameters were used for the 30 mm tube chambers, for the 15 mm tubes two voltages were investigated: 2730 V and 2760 V.
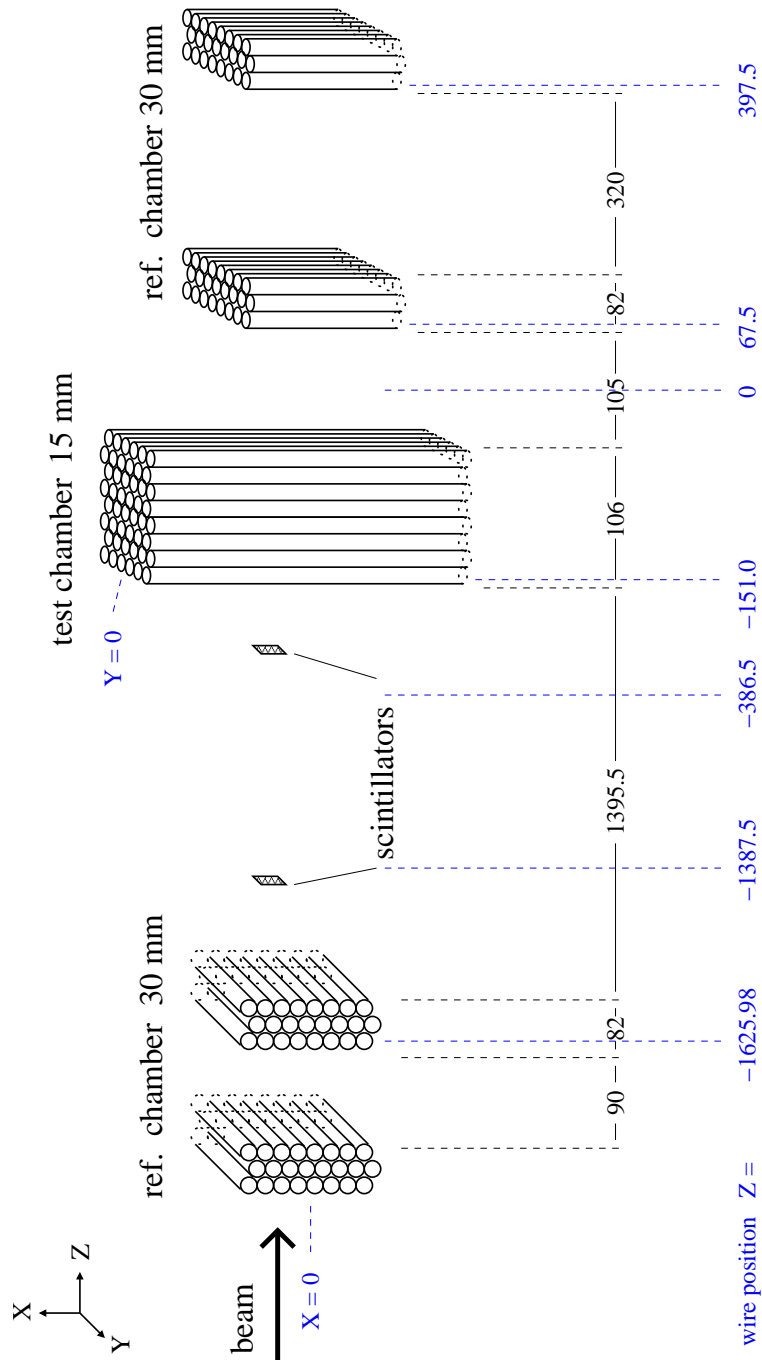
Figure 3.3: *The H8 setup at CERN: A prototype chamber of 96 tubes was tested with 140 GeV muons, only 15 o the 96 tubes were fully irradiated. Behind the 15 mm tube chamber, a chamber of 30 mm tubes provided reference tracking.*

4 DATA ANALYSIS

4.1 Drift Time Spectrum and Space-Time Relation

The drift time spectrum, as shown in fig. 4.1, provides the basic data for the analysis.

$\frac{\Delta N}{\Delta t}$, a bin of the spectrum, corresponds to

Eqn. 4.1:
$$\frac{\partial N}{\partial t} = \frac{\partial N}{\partial r} \frac{\partial r}{\partial t}.$$

Since the illumination level of a tube is very homogeneous, one assumes

Eqn. 4.2:
$$\frac{\partial N}{\partial r} \approx const,$$

and therefore

Eqn. 4.3:
$$\frac{\partial N}{\partial t} \sim \frac{\partial r}{\partial t}.$$

So the drift time spectrum expresses the drift velocity as a function of the drift time. The shape of the spectrum is characteristic for the drift properties of a tube.
To characterize the spectrum a fermi function
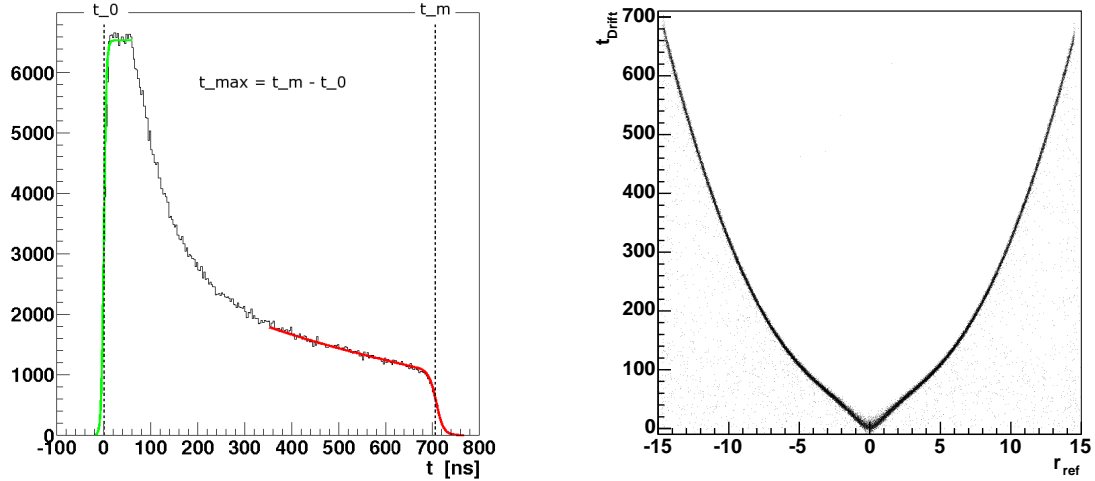
Figure 4.1: left: Drift time spectrum; right: rt-relation.

Eqn. 4.4:
$$F(t) = \frac{A_0}{1 + e^{\frac{t - t_0}{T_0}}}$$

is fitted to the rise of the drift time spectrum (cf. [34]). To the end of the drift time spectrum a similar function

Eqn. 4.5:
$$F(t) = \frac{A_m e^{a_m t}}{1 + e^{\frac{t - t_m}{T_m}}}$$

is fitted, which includes the descent of the spectrum before the trailing edge.

The inflexion point of the leading edge, given by t_0, must be subtracted from the measured time to obtain the drift time. The length of the spectrum $t_m - t_0$ is the maximum possible drift time and is mainly depending on gas mixture, pressure, temperature and electric field.

By integrating the drift time spectrum, one obtains an initial space-time (rt) relation. This roughly determined relation can be used as input for the precise rt calibration described in the next section.

4.2   Tracking and Autocalibration

The wire positions of the tubes are defined in the y-z-plane, where y runs along a tube layer and z gives the layer coordinate. The x axis is then in parallel to the anode wires of the tubes.
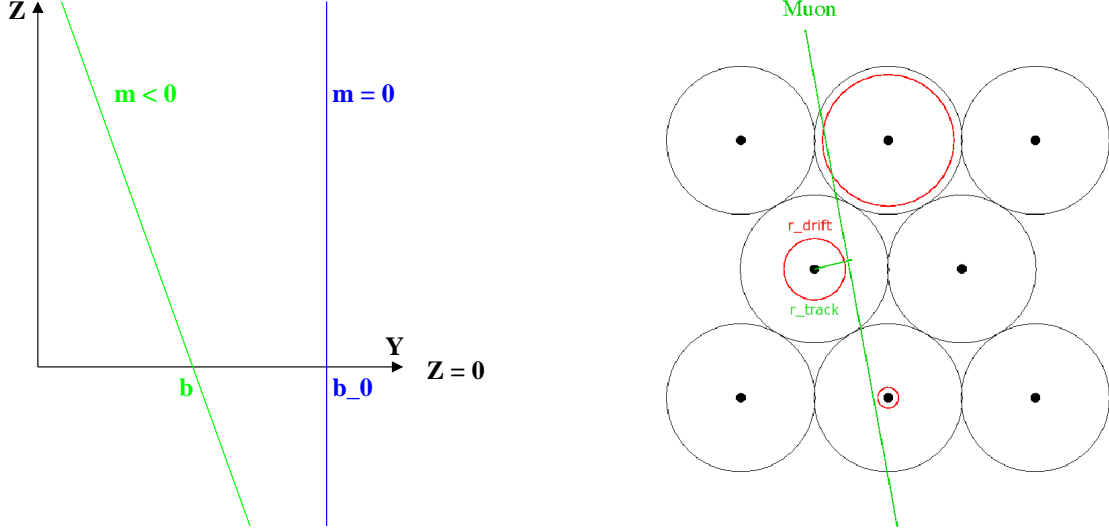
Figure 4.2: left: The coordinates and the parameters of a muon track; right: Scheme of tracking.

4.2.1   *Reconstruction of a Muon Track*

The path of a muon through a drift chamber is assumed to be a straight line with equation

Eqn. 4.6:
$$y = mz + b.$$

So the reconstruction of a muon track with n hit tubes is consistent with the minimization of [35]

Eqn. 4.7:
$$\chi^2 = \sum_{i=1}^{n} \frac{\left(r_{drift,i} - r_{track,i}\right)^2}{\sigma\left(r_{drift,i}\right)^2}.$$

The distance of the track to the wire in the ith tube is given by $r_{track,i}$, whereas $r_{drift,i}$ corresponds to the measured drift radius in this tube (fig. 4.2). The translation function to get the drift radius from the measured drift time will be explained in the next section. The single tube resolution $\sigma(r_{drift,i})$ is taken from earlier analysed data, namely millions of events taken at the CRMF in Garching (Munich). For the minimization of χ^2 the quasianalytical method, described in [35], is used. Herein the track parameters m and b are determined for pairs of hit tubes in different multilayers in so-called wire-wire coordinates. The slope and the intercept of the track are given by:

Eqn. 4.8:
$$m = \frac{r_2 - r_1}{\sqrt{L^2 - (r_2 - r_1)^2}}$$

and

Eqn. 4.9:
$$b = r_1 \sqrt{1 + \left(\frac{r_2 - r_1}{\sqrt{L^2 - (r_2 - r_1)^2}}\right)^2}.$$

The errors on the track parameter are then defined as:

Eqn. 4.10:
$$\delta m = \sqrt{\frac{L^4(\sigma_1^2 + \sigma_2^2)}{(\sqrt{L^2 - (r_2 - r_1)^2})^3}}$$

and

Eqn. 4.11:
$$\delta b = \sqrt{\frac{L^2(a + b)}{(\sqrt{L^2 - (r_2 - r_1)^2})^3}}\right)^{\frac{1}{2}},$$

with $a = \sigma_1^2 L^4 - 2\sigma_1^2 L^2 r_2^2 + 2\sigma_1^2 L^2 r_1 r_2 + \sigma_1^2 r_2^4 - 2\sigma_1^2 r_2^3 r_1 + \sigma_1^2 r_2^2 r_1^2$ and $b = \sigma_2^2 r_1^2 r_2^2 - 2\sigma_2^2 r_1^3 r_2 + \sigma_2^2 r_1^4$.

In the equations above, r_1 and r_2 are the measured drift radii, σ_1 and σ_2 the resolution for the radii and L the distance between the two wires. The final track parameters m and b are provided by the weighted mean of $b_{j,k}$ and $m_{j,k}$ according to:

Eqn. 4.12:
$$ m = \frac{\sum\limits_{j=1}^{n} \sum\limits_{k=j+1}^{n} \frac{m_{j,k}}{\sigma_{m,j,k}^2}}{\sum\limits_{j=1}^{n} \sum\limits_{k=j+1}^{n} \frac{1}{\sigma_{m,j,k}^2}} \text{ and } b = \frac{\sum\limits_{j=1}^{n} \sum\limits_{k=j+1}^{n} \frac{b_{j,k}}{\sigma_{b,j,k}^2}}{\sum\limits_{j=1}^{n} \sum\limits_{k=j+1}^{n} \frac{1}{\sigma_{b,j,k}^2}} \ , $$

where $\sigma_{b,j,k}$ and $\sigma_{m,j,k}$ are the uncertanties on $b_{j,k}$ and $m_{j,k}$.

Before the averageing all slopes and intercepts have to be transformed into the coordinate system of the setup. The transformation is described in [36]. To give a precise muon track, the covariance of the slope $m_{j,k}$ and the intercept $b_{j,k}$ must disappear, which is the case for large L. Therefore only tube pair combinations, which are in different multilayers are used. Due to that fact a track in a tube bundle will have large errors on the track parameters. This was the case at the H8 test beam (see chapter 6).

4.2.2 *Determination of the Space-Time Relation*

Drift tubes measure the time electrons need to arrive at the anode wire. For the determination of drift radii one needs a translation function, that provides the drift radius corresponding to the measured drift time. This relation is called space-time relation and can be determined with muon data for each chamber, if the track in a chamber is overdetermined.

As starting point either a rt-relation simulated with Garfield, a rt-relation of an earlier measurement or the rt-relation obtained by integrating the drift time spectrum is used. This rt-relation is realised as a data set of 23 sampling points with linear interpolation between these points.

A first tracking with the guessed rt-relation is performed. To iteratively improve this relation per multilayer or chamber, one plots the residual defined as

Eqn. 4.13:
$$res(t) = r_{drift}(t) - r_{track}(t)$$

versus r_{track} (shown in fig. 4.3). The mean values of the residuals in intervals of t provide the correction on the 23 sampling points of the rt-relation. So the improved relation is given by

Eqn. 4.14:
$$r'_{drift}(t) = r_{drift}(t) - \langle res(t) \rangle.$$

This algorithm is rerun until $\langle res(t) \rangle$ is smaller than 20 μm for all radii. Normally 3 iteration steps are needed. This method, therefore, autocalibrates a drift tube without need of external references. Hence this method is known as autocalibration [38, 39]. The residual distribution after the rt-calibration shows fig. 4.3.
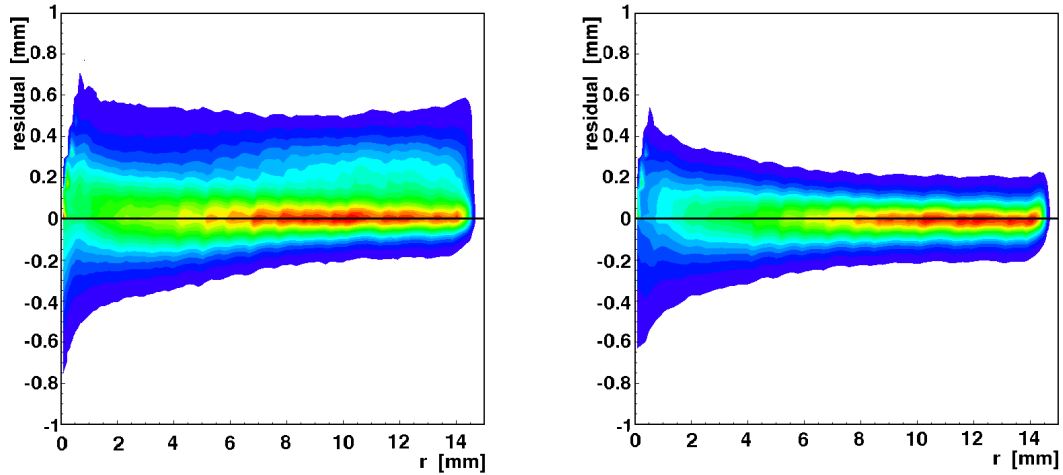
Figure 4.3: left: Residual before rt-calibration; right: residual after rt-calibration.

4.3 Alignment via Tracks

Although the two reference chambers in the GIF setup should be roughly aligned, analysing the data shows, that further geometrical corrections are needed. Possi-

ble corrections are discussed in this section.

Each track is given by

Eqn. 4.15:
$$y = mz + b$$

where m corresponds to the slope and b gives the y-axis intercept in case of $z = 0$.

Comparing the two tracks, reconstructed by the two reference chambers gives insight into the geometrical displacements. Herefore tracks reconstructed in the lower reference chamber are extrapolated into the upper reference chamber and vice versa. The residual distribution (see eqn. 4.13) versus radius looks characteristic for the different displacements (rotations or shifts).

4.3.1 *Residual Distributions using a Reference Track*

Shift of a Chamber

x-shift

With the setups described in this work, it is not possible to monitor a shift in x direction.

y-shift

Fig. 4.4 shows a y-shifted tube and the measured distance from the wire, where the track passes by, in case of positive and negative slopes and also including positive and negative drift radii. For a positive y-displacement all drift radii are measured wrongly. Positive drift radii are always smaller, whereas negative ones are always larger than they should be. Looking at the residual distribution as function of the radius, the distributions for negative and positive slopes are in agreement.
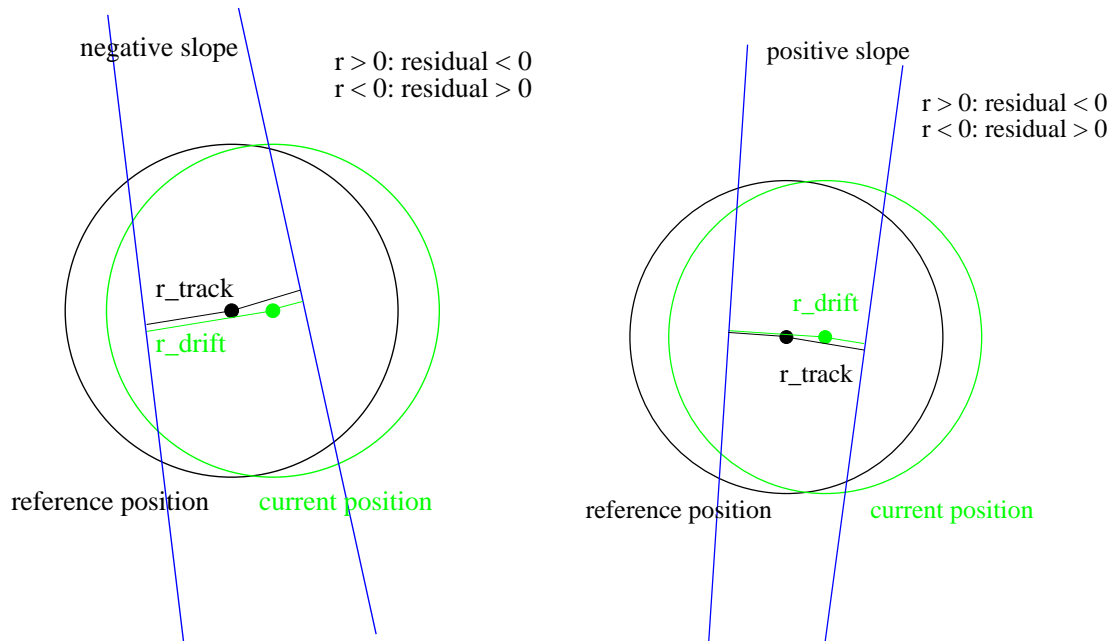
Figure 4.4: left: Scheme of a y-shift in case of tracks with negative slope; right: Scheme of a y-shift in case of tracks with positive slope.
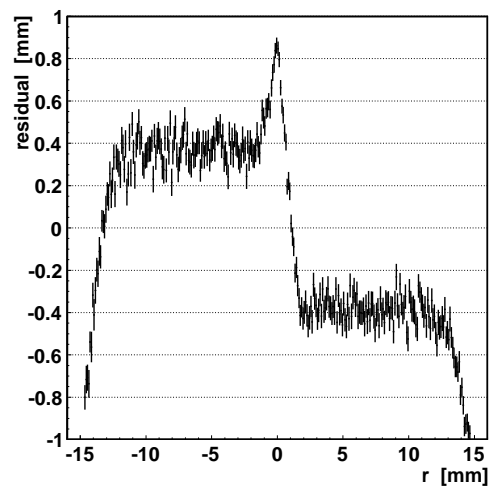
Figure 4.5: Residual for positive and negative slopes against the radius in case of a positive y-shift.

For a shift in positive y direction the residuals are positively shifted in case of negative radii and negatively for positive radii (fig. 4.5). The value of the amplitude of the shift is the same. If the shift is in negative direction, the value of the amplitude stays the same whereas the sign changes compared to the positive shift.

z-shift

A z-shift of a tube in positive z direction is shown in fig. 4.6. In case of positive slopes the track radius is measured too small for tracks passing on the negative wire side of the tube and measured too big concerning positive radii. Therefore one gets an asymmetric residual distribution with negative residuals for negative radii and positive residuals on the positive wire side (see fig. 4.7). The amplitude is the same.
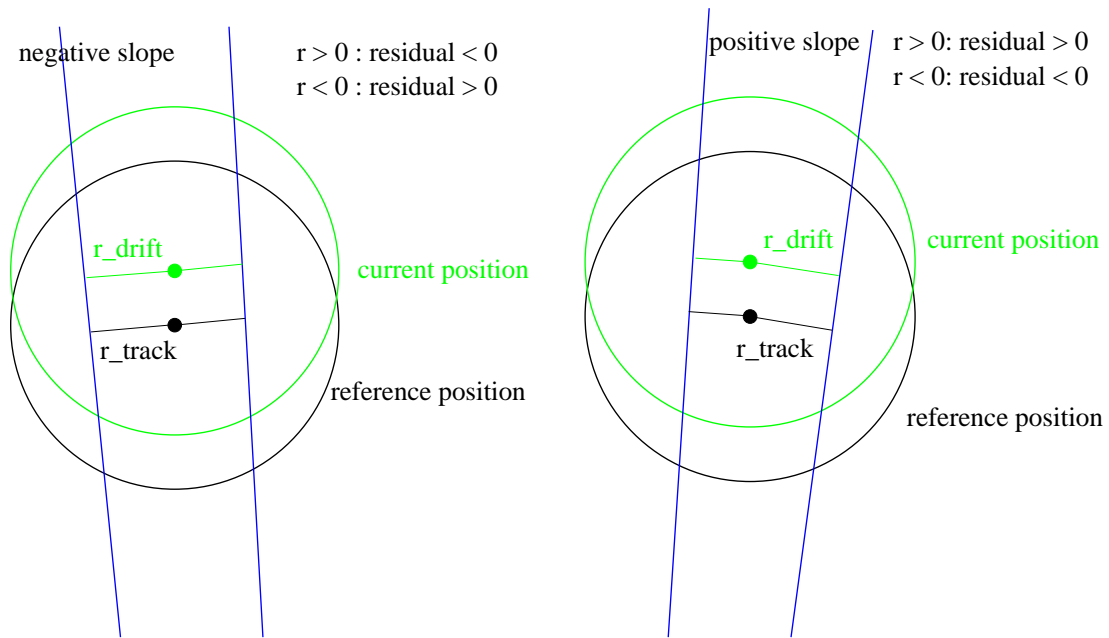
Figure 4.6: left: Scheme of a z-shift in case of tracks with negative slope; right: Scheme of a z-shift in case of tracks with positive slope.

Looking at negative slopes the residual distribution changes its sign compared to the positive case (fig. 4.7).
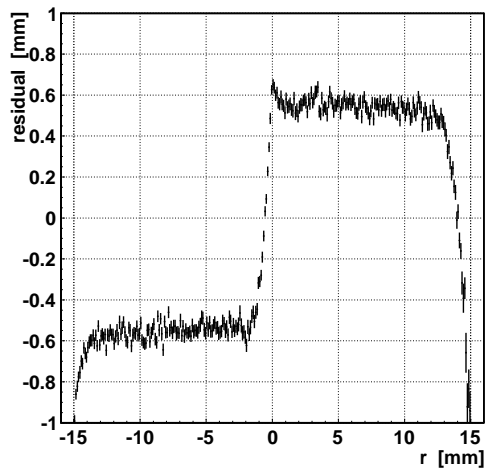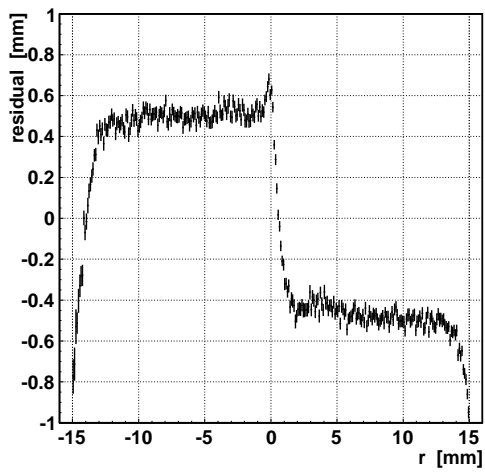
Figure 4.7: z-shift: left: Residual for negative slopes; right: Residual for positive slopes.

Rotation of a Chamber

Rotation in x along Chamber Axis

To see a possible positive rotation around x, one has to split the reference chamber into 4 parts. Every multilayer of a chamber is split into a part of positive and negative y of the local coordinates. The four parts are called leftup, rightup, leftlow and rightlow, as shown in fig. 4.8. The rotation axis is the center of gravity of a chamber.
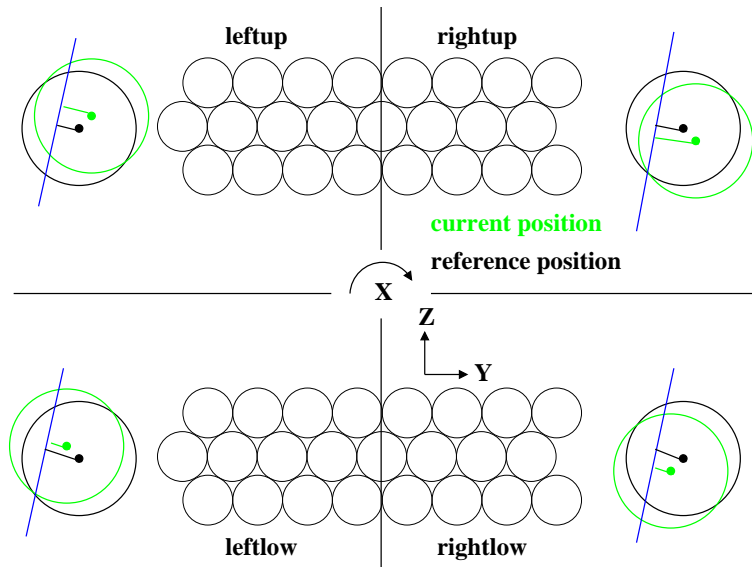
Figure 4.8: Scheme of a rotation around x. In this case the chamber is split into 4 parts. The measured radius is indicated for all sections (r_{drift} in green and r_{track} in black).

The x-rotation for a point on the chamber is an overlay of a y- and z-shift. Regarding one of the 4 sectors the wire shift direction is identical, but the shift value is different for each tube. The wire shift direction of a tube in each section is also shown in fig. 4.8. A chamber is rotated around x, if the residual distributions of leftup and rightup have the same shape for all slopes. For negative radii the mean of the residual is positively shifted and for positive radii negatively.

Looking into the distributions of rightlow and leftlow also the shape agrees, but now at positive radii the residual is negatively shifted and vice versa at negative

radii. The minimal shift in the residual corresponds to the tube wires next to the rotation axis and increases with the distance from the axis. This is valid for all four sectors of a chamber.

Looking at the rotation direction, one sees that all residual distributions change their sign in case of negative rotation.

Rotation in y: Tilt of Chamber

A rotation around the y axis has the same characteristics as a z-shift, but the amplitude and sign of the residual distributions differ at different x positions in a chamber. At the wire ends the amplitudes are maximal and only the sign is different. Going in x towards the chambers center of gravity the amplitude decreases and is zero at the coordinate origin.

Rotation in z: Wires are no longer in parallel

The rotation around the z-axis comes along with a signature similar to a y-shift. The sign of the residual shift is the same as in case of a y-shift. Looking at the residual distributions at different sections along the wire (x direction) the amplitude of this y-shift decreases to zero at the origin and increases with opposite sign until the other wire end is reached.

displacement	sign of residual shift	amplitude of residual shift
x-shift	no sensitivity	no sensitivity
y-shift	$r > 0 : res < 0 \ \forall$ slopes $r < 0 : res > 0 \ \forall$ slopes	$\lvert amp \rvert$ is equal $\forall$ slopes
z-shift	$r > 0 : res > 0 \ \forall$ pos slopes $r > 0 : res < 0 \ \forall$ neg slopes $r < 0 : res < 0 \ \forall$ pos slopes $r < 0 : res > 0 \ \forall$ neg slopes	$\lvert amp \rvert$ is equal $\forall$ slopes
rotation around x	overlay of y- and z-shift	$\lvert amp \rvert$ increases with distance of the wire from the rotation axis
rotation around y	like z-shift	$\lvert amp \rvert$ changes along wire
rotation around z	like y-shift	$\lvert amp \rvert$ changes along wire

Table 4.1: Characteristic shapes of chamber displacements in the residual distributions.

These displacements may also occur between the two multilayers of a chamber. In this case one has to look into the residual distributions determined with the track in this chamber.

Tab. 4.1 summarizes the characteristic shapes of chamber displacements in the residual distributions.

4.3.2 Track Parameter Distributions

If there exist two reconstructed tracks, one can use the differences of the parameters m and b of the two tracks $y = mz + b$ to determine displacements. These distributions are shown in fig. 4.9.

Regarding the difference of the y intercept, the y-shift is given by the mean of this distribution. The slope difference yields the rotation angle around x. To distinguish a possible z-shift one analyses the z difference given by:

$$\textit{Eqn. 4.16:} \qquad dz = \frac{b_1 - b_0}{slope},$$

with b_1 and b_2 being the intercepts of the two tracks. Due to the fact that for small slopes a y difference translates into a large z difference, the distribution is broad and the alignment accuracy for this coordinate is bad. In case of a larger y-shift, the z difference also changes characteristically by getting broader or, depending on the binning, showing two peaks.

4.3.3 Alignment Track to Track Comparing 2 Chambers

A second possibility to align two chambers is to transform tracking parameters. This method is described in [29] and was adapted. Regarding the y-z-plane, which is perpendicular to the wires, there are three possible displacements, namely a y-shift, a z-shift or a rotation around x.

Using this method, one assumes that both chambers are built according to nominal wire positions. One chamber measures reference tracks, assumed to deliver true tracking parameters. The other chamber is analysed using the nominal geometry.
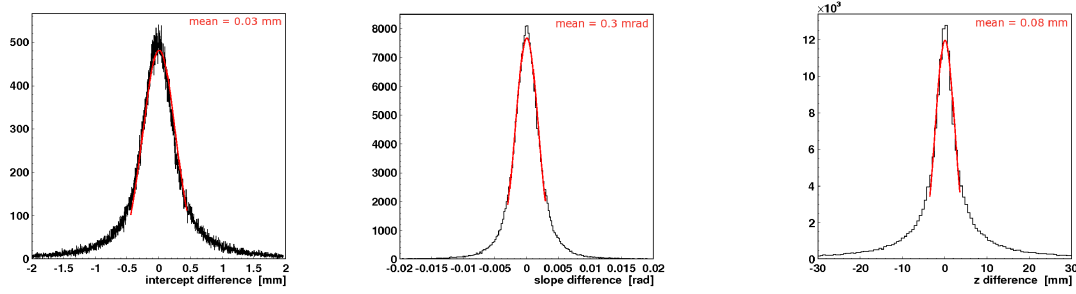
Figure 4.9: The mean of the intercept difference (left) of two tracks yields the y-shift and the mean of the slope difference (middle) gives the rotation angle around x. The right plot shows the difference in z and the mean yields the correction value for a z-shift.

Due to that, systematic deviations between the nominal track and the true track can be observed.

A track is defined as

Eqn. 4.17:
$$y = mz_{n/t} + b_{n/t},$$

where n is the index for the nominal track and t for the true one.

Assuming that only one deviation is present, the y-shift is given by the difference of the y intercept

Eqn. 4.18:
$$\Delta y = b_t - b_n.$$

The rotation around x comes along with a deviation in the slopes:

Eqn. 4.19:
$$\alpha = m_t - m_n.$$

where α is the rotation angle using small-angle-approximation. In case of a z-shift the deviation depends on the the slope:

Eqn. 4.20:
$$\Delta z = \frac{b_t - b_n}{m_t}.$$

Regarding 3 dimensions, also rotations around y (β) and z (γ) and a drilling of the chamber t are possible. These deviations show up with the change of Δy, Δz and α along the wire, i.e. along the x direction. These changes are described via:

Eqn. 4.21:
$$
\begin{aligned}
t &= \frac{\partial}{\partial x}\alpha \\
\beta &= \frac{\partial}{\partial x}\Delta y \\
\gamma &= \frac{\partial}{\partial x}\Delta z
\end{aligned}
$$

To extract the values for the displacements from the data, two distributions are fitted. The rotation angle α is given by the mean of a gaussian fitted to the slope difference (fig. 4.9, left), according to eqn. 4.19.

As it can be seen in eqns. 4.18 and 4.20, Δy and Δz are defined by the intercept difference. The 2 dimensional distribution of the intercept difference (see fig. 4.10) against the slope is fitted with a straight line. The slope of this fit function yields Δz and the intercept of it gives Δy.

Using a segmented hodoscope one is able to determine and plot these three parameters as function of x (track position along the wire). Adapting straight lines to these distributions yields the correction parameters α_0, Δy_0, Δz_0 via the intercepts and β, γ and the drilling t via the slopes. These values define the relative position of the reference chamber to the test chamber, reconstructing the true track.
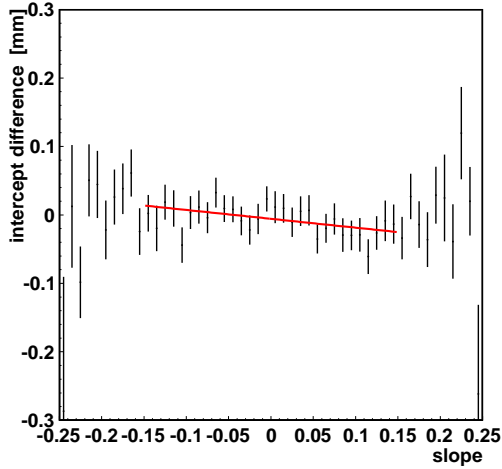
*Figure 4.10: A straight line fit to the intercept difference plotted against the slope yields
Δy (intercept for slope $= 0$) and Δz (slope of fit).*

Transforming the slope and the intercept according to

Eqn. 4.22:
$$\begin{aligned} m' &= m + (\alpha_0 + tx) \\ b' &= b + (\Delta y_0 + \gamma x) - m(\Delta z_0 + \beta x), \end{aligned}$$

the true track is given by

Eqn. 4.23:
$$y = m'z + b'.$$

All discussed deviations are only valid exactly, if the chamber deviates in one
degree of freedom. This implies that this method has to be executed iteratively
until the determined values are smaller than the errors on the fits.

4.4 Resolution

Resolution is among the main performance parameter for drift tube chambers.

The single tube resolution is determined using the residual distribution of a tube or layer, depending on the present statistics. The inspected tubes are not included in the track fit. The residuals are projected in slices of r and then fitted using a double gaussian [40]:

Eqn. 4.24:
$$fit = a \cdot exp\left(-\frac{1}{2}\left(\frac{x-\mu}{\sigma}\right)^2\right) + b \cdot \exp\left(-\frac{1}{2}\left(\frac{x-\mu}{3\sigma}\right)^2\right),$$

where the broader gaussian distribution with $3\,\sigma$ describes the tails caused mainly by δ-electrons. This is shown in fig. 4.11. The σ of the gaussian is then equivalent to the resolution for the regarded slice in r. To deal with an the statistical uncertainty of few percent level, the number of events per slice must exceed 1000 and the typical slice size is 0.5 to 1 mm.
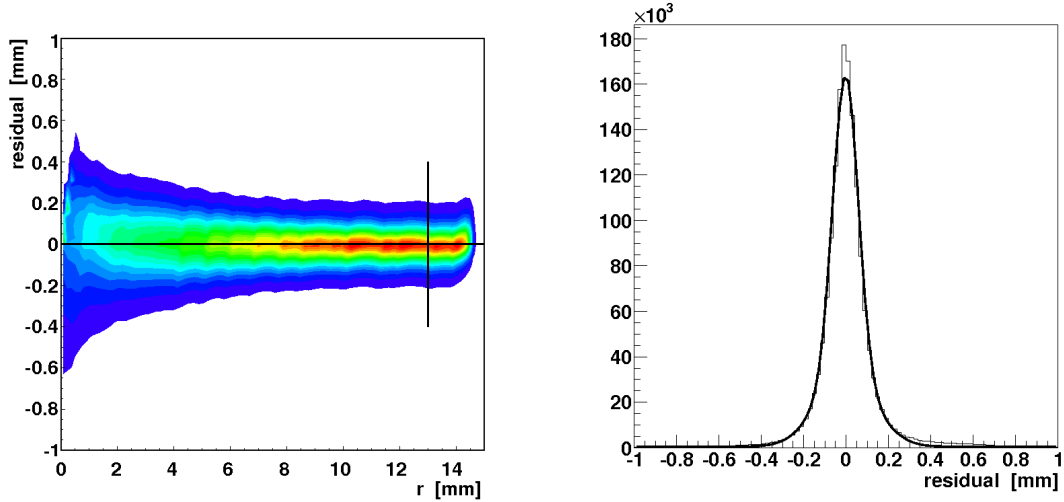
Figure 4.11: left: Residual distribution for 5 million events; right: residual projection for a slice around 13 mm ± 0.5 mm with 0.35 million events.

5 ALTERNATIVE DRIFT GASES

Aiming towards a better performance of the muon spectrometer at the ATLAS experiment at high luminosities, a faster and more linear drift gas can provide more precise muon tracking at higher background rates. Using a faster gas mixture reduces the dead time of the electronics and thus occupancy, as less muon tracks will be lost due to background hits occupying a tube. The linearity of the rt-relation reduces the dependence of the electron drift on changes of the electric field in a tube due to space charges.

5.1 Gas Mixtures

The studied alternative gas mixtures were chosen regarding the following aspects:

- linearity

- fastness

- inertess of gas components

- small streamer rate

- small afterpulsing.

Studies of different gas mixtures, simulations and measurements [41, 42], show that reducing the CO_2 content from 7 % in $Ar:CO_2$ mixtures makes the gas faster and more linear. The fastest gases are mixtures containing 3 Vol % of CO_2 (see fig. 5.1).

Regarding the linearity of these gas mixtures, shown in fig. 5.1 on the right, favoured gases contain 2 - 3 Vol % of CO_2.
Measurements showed, that gas mixtures of $Ar:CO_2$ show small afterpulsing behaviour in CO_2 Vol % range of 3 to 7. By adding a small amount of N_2, the afterpulsing is reduced furthermore. The measured streamer fractions are 4 % for the ATLAS gas and about 4.5 % for gas mixtures containing 1 % of N_2 [42].
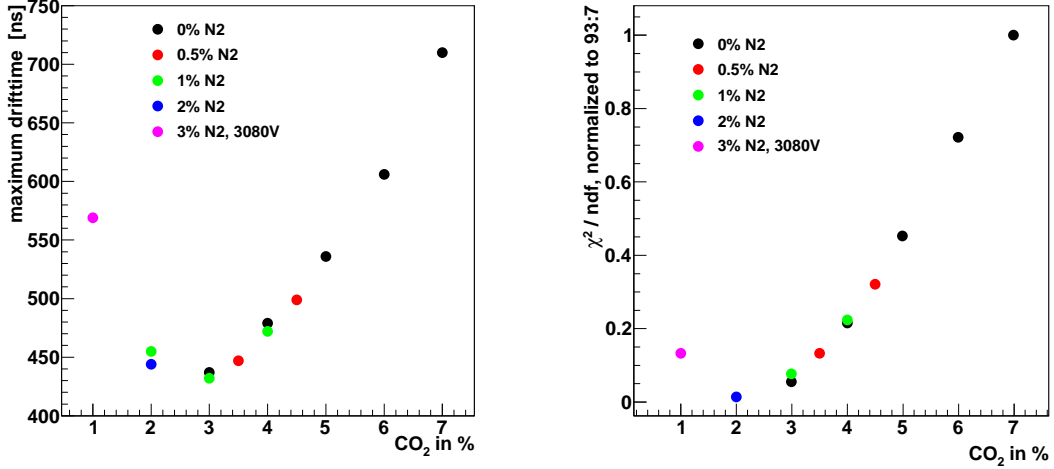
Figure 5.1: left: Maximum drift time of different gas mixtures against the amount of CO_2 and N_2. right: Linearity of different gas mixtures against the amount of CO_2 and N_2. [42]

Therefore the mixture of $Ar : CO_2 : N_2$ in the ratio of $96 : 3 : 1$ Vol % is a reasonable candidate to be tested for its performance under high radiation conditions. The maximum drift time (see fig. 5.2, left) of this mixture is with a value of 450 ns a factor of 1.5 faster than the ATLAS gas and by far more linear.

5.2 Performance

5.2.1 *Cosmic Ray Measurement Facility*

At the cosmic ray measurement facility (CRMF) in Garching two gas mixtures containing N_2, namely $Ar : CO_2 : N_2$ in a ratio of $96 : 3 : 1$ Vol % and $97 : 2 : 1$ Vol % were tested at standard ATLAS conditions. Cosmic muons were used to determine the resolution of the gas mixtures. The amount of collected events differed. 45 million muons for the standard gas, 35 million for the mixture $96 : 3 : 1$ and 3 million for the mixture $97 : 2 : 1$.

The position resolution is shown in fig. 5.2 on the right side. Both tested gas mixtures show similar single tube resolution compared to the standard gas [45].

At small radii the resolution is in the range of 200 μm. The N_2 mixtures show here better resolution, which is caused by a higher gas gain, as the high voltage on
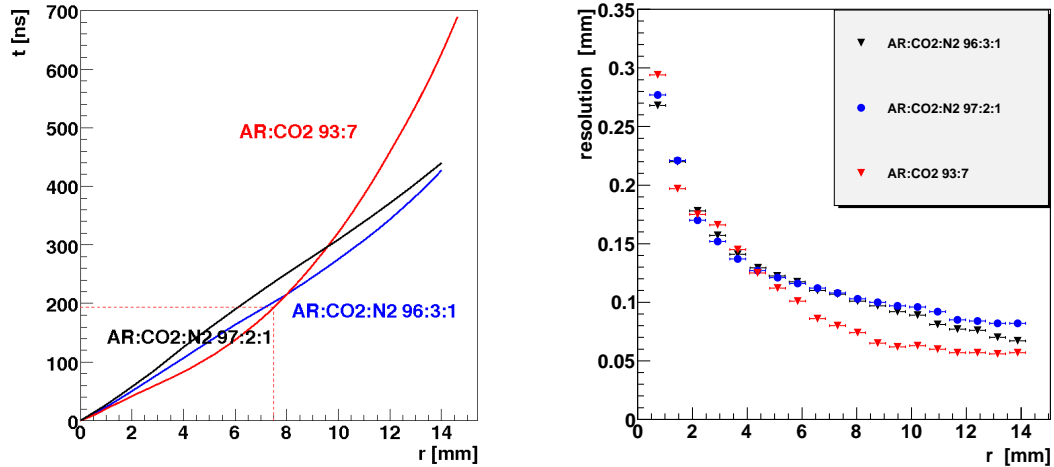
Figure 5.2: left: Measured rt-relations of the three gas mixtures. The alternative mixtures are faster and more linear. right: The measured resolution of two gas mixtures containing N_2 and the standard gas are similar.

the anode wire was the same for all mixtures. The pulse height spectrum (fig. 5.3) shows, that the maximum of the spectrum is shifted to a higher value. The gas gain is about 7 % higher using the alternative gas mixtures. Regarding bigger radii the standard gas shows better resolution due to a smaller drift velocity in this region. The measured resolution of the alternative gases fulfill the ATLAS requirements of an average resolution better than 100 μm.

The gas mixture $Ar : CO_2 : N_2$ in a ratio of $96 : 3 : 1$ was also tested under high rate conditions. This measurement is described in the following.

5.2.2   *Gamma Irradiation Facility*

Drifttime Spectra and rt-Relation

Fig. 5.4 shows the drifttime spectrum and rt-relation of the ATLAS gas $Ar : CO_2$ $93 : 7$ and $Ar : CO_2 : N_2$ $96 : 3 : 1$ measured in the GIF setup without γ background. Both gases show a steep rise in the drift time spectrum and the alternative mixture has a more rectangular shape. It is visible that the alternative gas mixture is faster and more linear than the standard gas. The maximum drift time of the alternative gas is 450 ns compared to 700 ns of the standard gas.
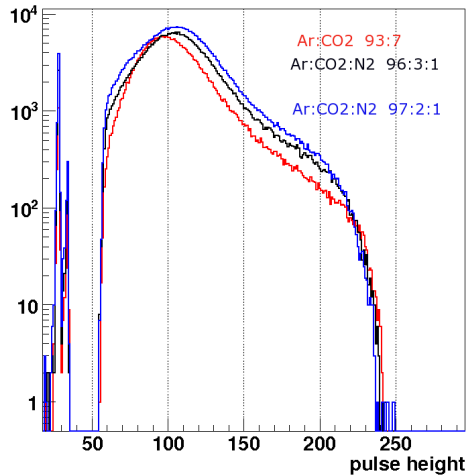
Figure 5.3: *The pulse heigth of the three gas mixtures in the test. The mean of the spectrum is at larger values for the two gas mixtures containing N_2, indicating a higher gas gain.*

Muon Track Reconstruction

The muon tracks in the lower and upper reference chambers are reconstructed separately using the methods described in chapter 4 and rt-relations were determinded for each multilayer of tubes. Fig. 5.5 shows the y-intercept and the slope of the muon tracks passing the setup.

The distribution of both parameters shows for both chambers almost identical shape. The range of the y-intercept, from - 120 to 125 mm, corresponds to the width of the reference chambers of about 255 mm. The peak on the right edge as well as the fact that the width of the y-intercept is about 10 mm smaller than the width of the chamber is caused by the asymmetry of a reference chamber, where the middle tube layer of each multilayer is shifted by half the tube radius. The peak in the red distribution is higher. Because of the smaller distance of the tube multilayers in the lower chamber the probability for both outermost tubes of the shifted layers being hit is larger.

The distributions of the slope are axially symmetric and the maximum values of about 0.25 mirror the geometric boundaries due to the hodoscope. The maximum possible slope using the distance and the width of the trigger hodoscope ($d = 1120$ mm and $b = 280$ mm) leads to a value of $tan\theta = 0.25$.
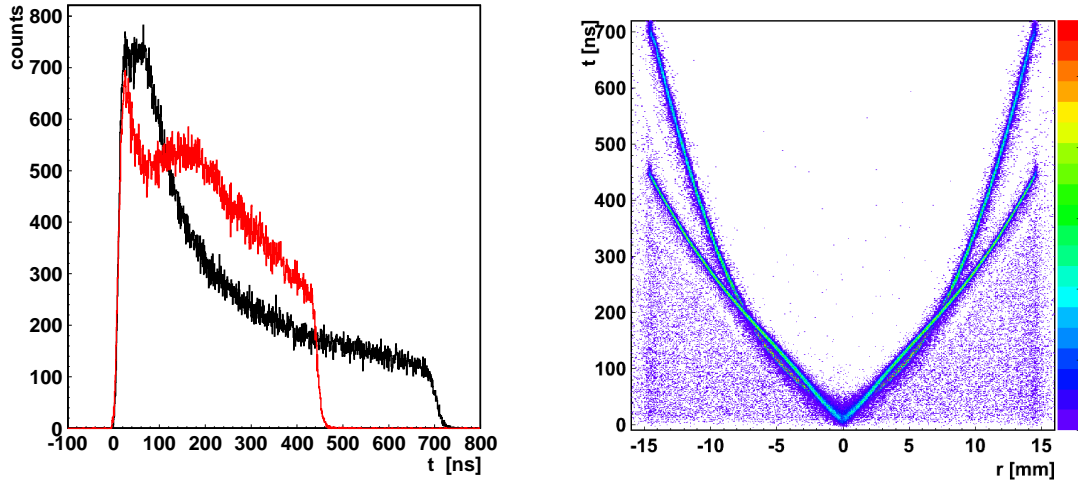
Figure 5.4: left: Drift time spectra of $Ar:CO_2:N_2$ $96:3:1$ and $Ar:CO_2$ $93:7$. One observes a steep rise for both gases. The shape of the N_2 gas mixture is more rectangular, which is characteristic for linear gases. right: The rt-relation for both gases show that the N_2 mixture is faster (450 ns compared to 700 ns) and by far more linear.

The distributions of the absolute errors on the track fit parameters are shown in fig. 5.6. Expectedly, due to the different distance between the multilayers of the chambers, 320 mm for the upper 30 mm chamber and 90 mm for the lower one, the errors on the reconstructed track in the lower reference chamber are bigger than in the upper chamber and the distribution is broader in the lower chamber. Considering the mean of the distributions, the upper track fit is, because of the lever arm, by a factor of 2.3 more precise than the lower one. Dividing 402 mm by 172 mm, which are the distances of the middle layers of the multilayers, yields also 2.3 as the measured ratio. This fact has to be kept in mind for error corrections in case of extrapolating tracks into the other chamber. For the upper chamber the accuracy on the slope is $3.74 \cdot 10^{-4}$ and 102 μm on the intercept. Whereas the lower track fit has $8.88 \cdot 10^{-4}$ slope error and 235 μm intercept error.

The correlation plot between the slope and the intercept of a track gives information whether all software channels of the tubes and the hodoscope are correctly linked with the hardware channels and whether all channels were correctly working during the measurement. In case of a perfectly symmetric setup the plot should look rectangular and the two axes of symmetry should be the straight lines with $slope = 0$ and $intercept = 0$.
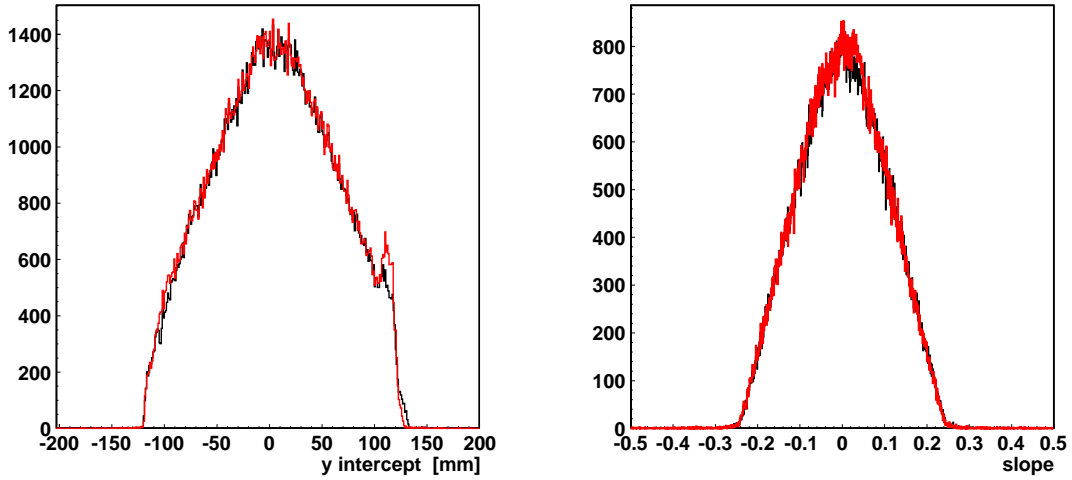
Figure 5.5: *The muon track fit parameters for $y = mz + b$ are shown for the upper (black) and lower reference chamber (red); left: y intercept (b), right: slope (m). Both distributions are in good agreement, which is equivalent to a reasonable initial alignment.*

The left plot of fig. 5.7 shows the correlation. One can see that it is approximately a parallelogram. The reason for the asymmetry is the non symmetric setup. The distance in z direction from the origin to the hodoscope layers differs. It is 575 mm to the upper layer and 545 mm to the lower layer. It generates the shift of the upper and lower corner by 15 mm. The multilayer assembly of the chambers with the shifted middle layer breaks the symmetry and causes the accumulation of data points in fig. 5.5 and the cutout near the right corner in fig. 5.7.

Looking at the right plot of fig. 5.7, one sees two bands with a low amount of data. In this case two out of seven scintillation counters in parallel to the tube wires were not operating in the lower hodoscope and therefore no muons could have been triggered in these regions. The two non operating counters were the ones next to the central counter, which is responsible for the band of data points in the middle.

The upper cut out band's corners are at $slope = -0.069$, $y = -90.7$ mm and $slope = -0.104$, $y = -71.6$ mm for the lower edge and for the upper edge at $slope = 0.175$, $y = 35.3$ mm and $slope = 0.142$, $y = 54.9$ mm. So the width in y is 19.35 ± 0.25 mm and for the $slope$ 0.034 ± 0.001. Calculating the expected width y_{miss} of a band due to a missing scintillation counter via
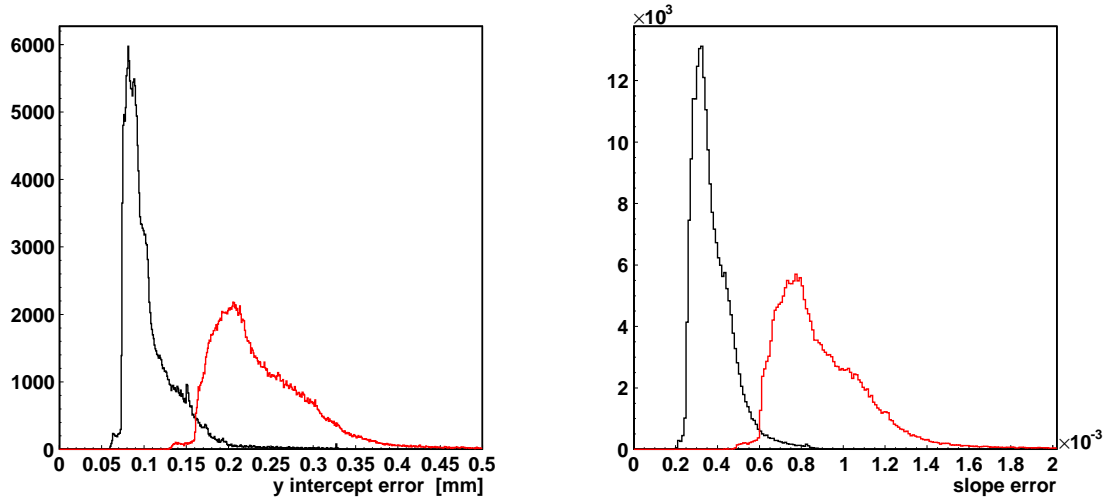
Figure 5.6: The errors on the muon track fit parameters are shown for the upper (black) and lower reference chamber (red). The errors are derived from eqns. 4.10 and 4.11 in chapter 4; left: y intercept, right: slope.

Eqn. 5.1:
$$y_{miss} = \frac{d_{hodo}}{d}b,$$

where $d_{hodo} = 545$ mm is the distance of the hodoscope to the origin, $b = 40$ mm the width of a scintillation counter and $d = 1120$ mm the distance between the two hodoscopes, yields approximately 19.46 mm in agreement with the measurement. The slope cutout width was calculated according to

Eqn. 5.2:
$$m_{miss} = \frac{b}{d}$$

and the value is 0.0357.

Alignment with Muon Tracks

At high background rates the track reconstruction becomes tough due to high occupancy of the irradiated multilayers. To determine the resolution under γ-background, extrapolated tracks reconstructed with the shielded multilayers were
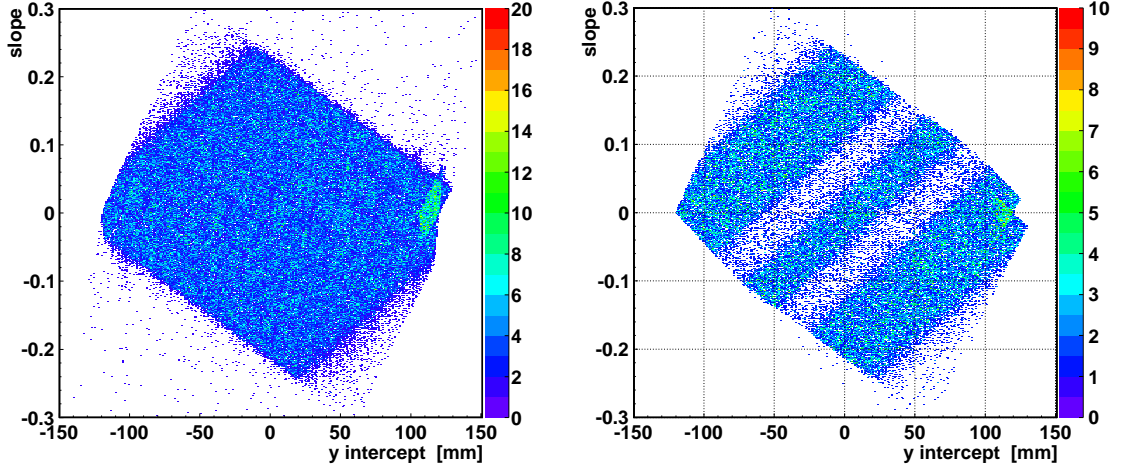
Figure 5.7: Correlation between the slope and the intercept of the muon track. left: normal distribution with quasi-rectangular shape; right: two scintillation counters of the lower hodoscope, parallel to the wires, were not operating.

used. Before that the two chambers have to be aligned internally and mutually. This was done comparing tracks and their extrapolation in case of no irradiation.

For a possible displacement of the multilayers of one chamber, the residual distributions were checked for the features described in section 4.3. They are investigated on asymmetric shifts of the mean for positive and negative radii for the five sectors along the wires given by the trigger hodoscope. Fig 5.8 shows no asymmetric shift for neither positive nor negative slopes. The average shift of the mean of about 30 μm in the middle of the chamber is within the production tolerance of the chambers.

The neglectable remaining deviation is not due to a wire sag effect in combination with further sag due to the electric potential, as the theoretically predicted value for the sag is around 3.3 μm and the additional sag due to electric field effects is at percent level of the nominal sag [43]. The sag was calculated via

Eqn. 5.3: $$z(x) = \frac{H}{q_0}\left(1 - cosh\left(\frac{q_0(x - L/2)}{H}\right)\right) - \frac{q_0 L^2}{8H}, q_0 = \pi r^2 \rho g,$$

where $H = 3.5$ N is the wire tension, $L = 50$ cm the length of a tube and $\rho = 19.17\frac{\text{g}}{\text{cm}^3}$ [44] the density of the W-Re wire.
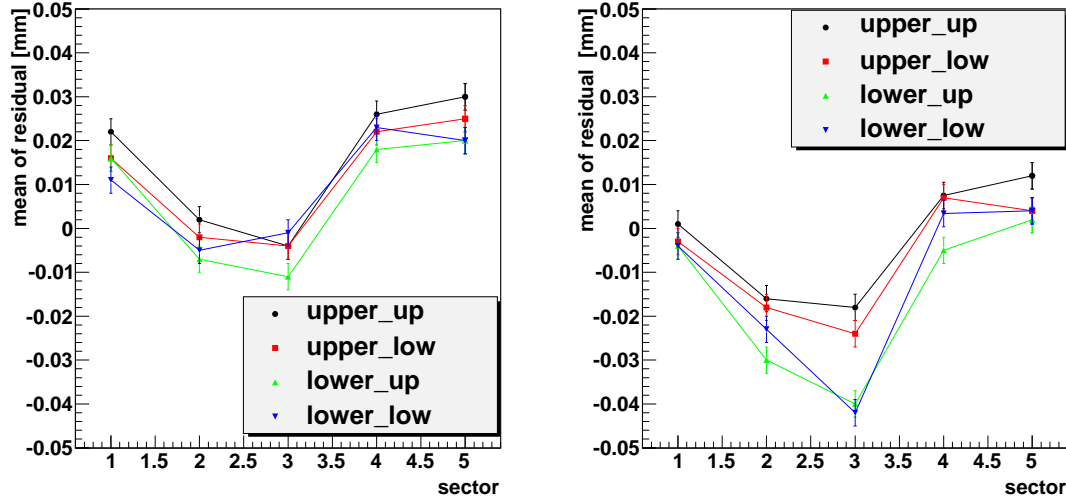
Figure 5.8: Mean of residual distribution of single multilayers along the wire. The left plot is for positive track slopes, the right one for negative slopes. The sectors are 10 cm broad and selected via the segmented hodoscope.

So both chambers show no abnormal geometrical deformation, which needs to be corrected.

Correction of Wire Position

Assuming that the geometry of the 30 mm tube chambers are perfect, one starts with 3 degrees of freedom for the alignment (2 dimensional case, not yet considering asymmetries along the wire). Namely a y-shift, a z-shift and a rotation around x.

The mean value of the gaussian distribution of the slope difference provides the angle for the rotational correction (fig. 5.9, left). A rotation of about 0.8 mrad, corresponding to a misalignment of about 130 μm, was performed. The difference of the intercepts gave a correction value of 190 μm for the y-shift (fig. 5.9, right). The correction of a z-shift of 67 μm was deduced from the 2-dim distribution dz against slope, see fig. 5.10.

After all corrections the alignment accuracy is better than 10 μm in y-direction (fig. 5.9) and 30 μm in z-direction (fig. 5.10).
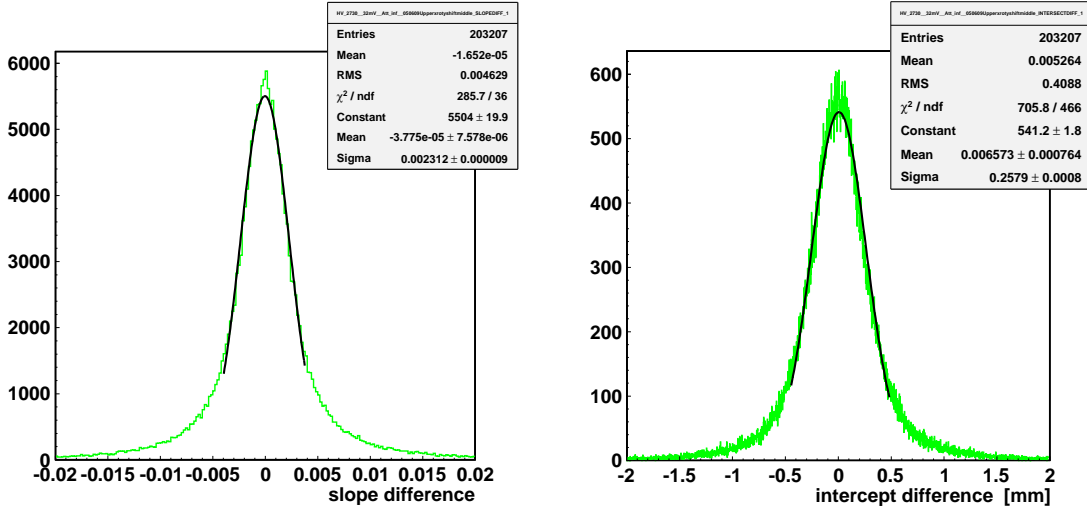
*Figure 5.9: Difference between the parameters of the two separatly reconstructed tracks;
left: slope, right: intercept.*

In the second step discrepancies in the alignment along the wire (3 dimensional) were investigated. Due to the geometry of the segmented hodoscope, one is able to extract tracks in 5 slices of 10 cm each along the wire. For the central region (section 3) the alignment is fine. But in section 1 and 5, at the ends of the tubes, one sees a further x-rotation. Fig. 5.11 shows, that section 1 is rotated positively and section 5 negatively compared to the middle of the chamber. The value of the shift in the intercept difference, also shown in fig. 5.11, is in agreement with a rotation of + 0.8 mrad on the one end of the chamber and - 0.8 mrad on the other end.

These results indicate, that one of the chambers is drilled along the x axis. The drill factor is 4.0 $\frac{\mu rad}{mm}$. Looking at the residual distributions in both chambers, one sees that in the upper chamber the residuals increase with the same sign from the lower multilayer to the upper multilayer as expected due to extrapolation. Whereas the extrapolation into the lower chamber yields a change of the sign in the residual's mean of the lower and the upper multilayer. So the lower 30 mm chamber is drilled. Using these informations the wire positions in all tubes were adapted.
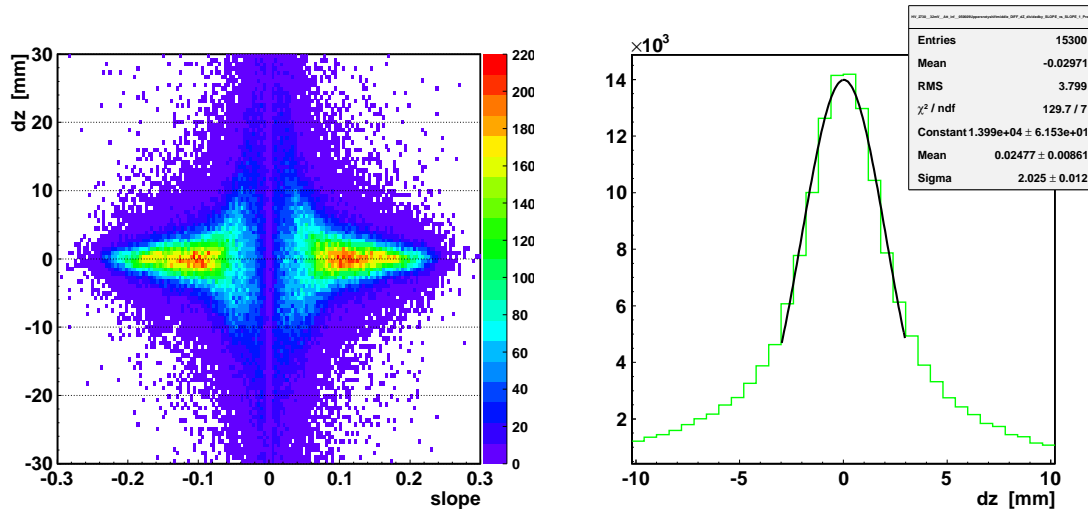
Figure 5.10: dz versus slope; left: 2-dim distribution, right: projection.
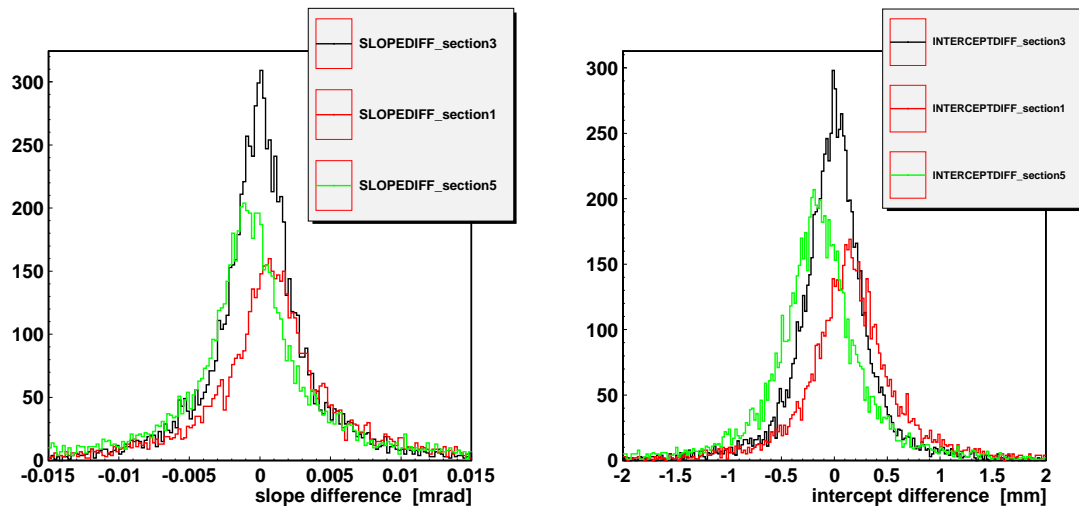
Figure 5.11: left: Slope difference along wire; right: intercept difference along wire.

Track to Track Correction

To confirm the alignment, gained with the method described before, the track to track alignment, as described in chapter 4, was additionally applied. Accordingly the lower track is considered to be correct and the upper track is transformed to fit the lower track. The correction is performed iteratively. Fig. 5.12 shows the
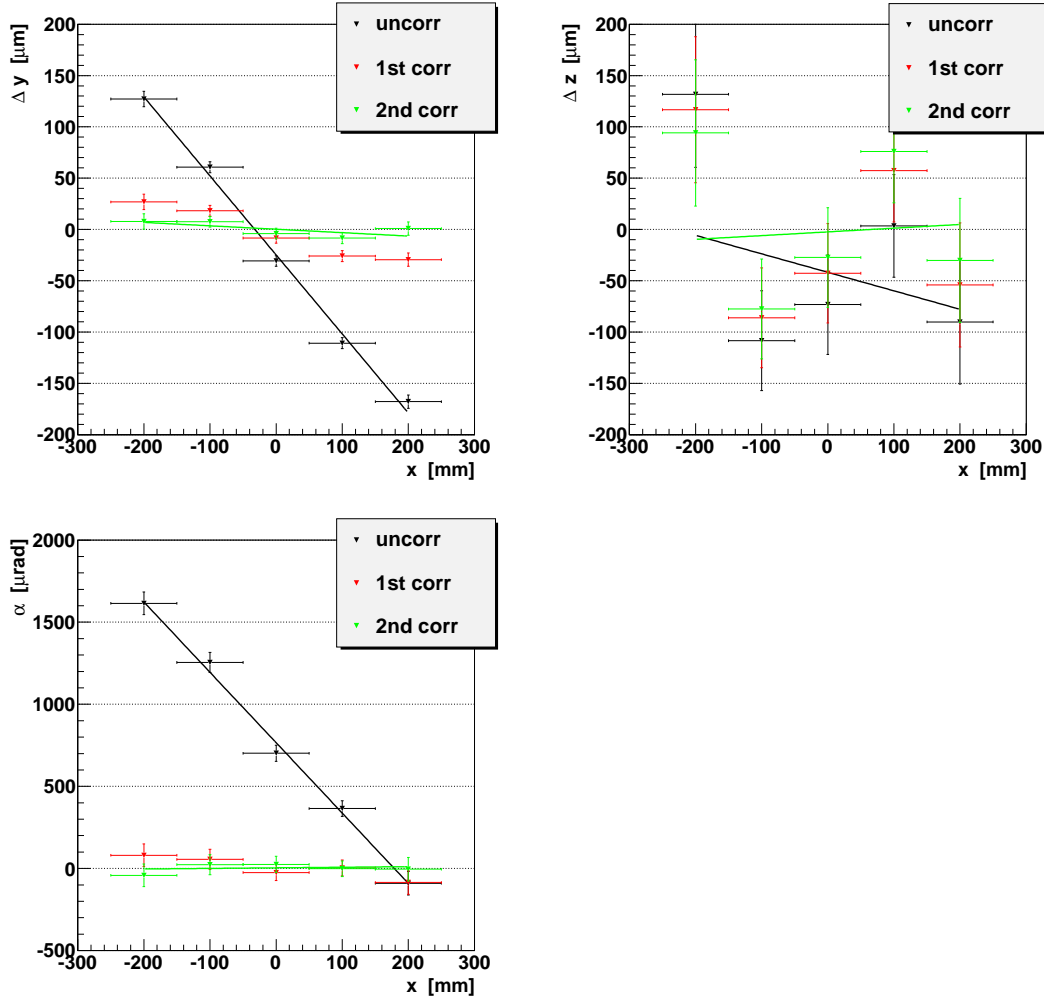
Figure 5.12: Δy, Δz and α plotted against the x position (along the wire) for the iteration steps. Straight line fits provide the correction values.

shifts in y-, z-direction and α as a function of x before the correction and after the 1st and 2nd iteration. A straight line fit to the data points show, that the drill of the chamber along x is 4.29 $\frac{\mu\mathrm{rad}}{\mathrm{mm}}$, the shift in y is 191 μm and in z 66.6 μm. These values are in agreement with the values determined using the other analysis.

Resolution

The resolution was determined following the scheme described in chapter 4.5. The result is plotted against the radius and shown in fig. 5.13 in case of no γ-background. As already seen in the results of the measurement at the CRMF, the resolution of the gas mixture $Ar:CO_2:N_2$ in a ratio of $96:3:1$ is similar to the standard mixture $Ar:CO_2$ $93:7$. The resolution ranges from about 250 μm near the anode wire to 70 μm near the tube wall. It is slightly worse at big radii due to different drift velocities in this region and better at small radii due to the higher gas gain as the voltage on the anode wire was the same for both mixtures. This measurement is in agreement with the result from the CRMF.
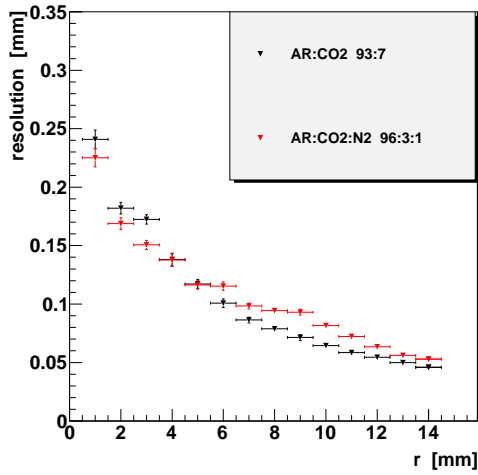
Figure 5.13: Single tube resolution of $Ar:CO_2:N_2$ 96:3:1 and the standard gas 93:7. The track resolution according to eqn. 5.4 is subtracted.

The average resolution of a reference track, extrapolated into the investigated tube, is determined via

Eqn. 5.4:
$$\langle \sigma \rangle = \sqrt{\frac{\sum_{i=1}^{n} \sigma_i^2}{n}}$$

and is shown in fig. 5.14. Herein σ_i is the resolution of the ith measured radius and n is the number of tubes used for the track fit. One sees, that the average

66

resolution of the reference track does not depend on the hit radius of the muon in the tube under investigation. Therefore no weighted correction on the single tube resolution has to be performed as function of the radius. The mean value of the distribution is 114 μm and the peak is 94 μm (fig. 5.14, left). The accuracy of the tracking, given by $\frac{\langle\sigma\rangle}{\sqrt{n-1}}$, is then 42 μm.
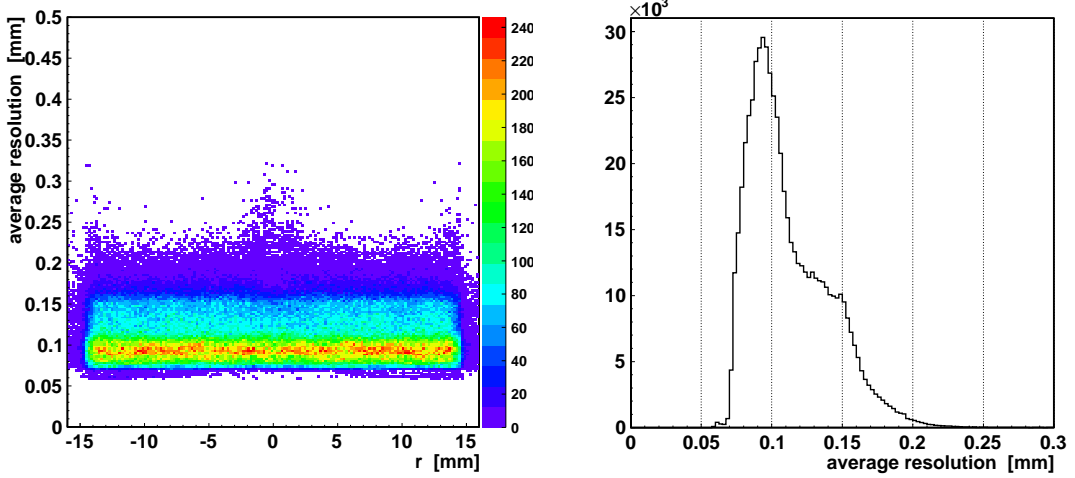
Figure 5.14: Average resolution as function of the tube radius (left) and the distribution of the average resolution (right).

5.3 Performance at High Rates

The presence of γ-background changes the drift field and therefore the drift spectrum. Fig. 5.15 shows the overlay of the drift time spectrum with and without background. The background rate of 662 keV γ was 295 $\frac{\text{kHz}}{\text{tube}}$, i.e. 1900 $\frac{\text{Hz}}{\text{cm}^2}$. At this γ-rate space charges are present in each tube at all time. The position of the ion charge ring in the tube causes then field fluctuations. Under this condition the maximum drift time of the standard gas decreases by 90 ns.

One sees furthermore, that the shape of the spectra differs. The rising edge is broader in case of γ-background. Due to the decreased electric field, the gas amplification is lower and less charges are produced. Therefore the crossing of the discriminator threshold is shifted and the drift time is determined later.

Field fluctuations are responsible, that the shape differs significantly at higher drift times and the falling edge gets broader. The non-linearity of the gas mixture

67
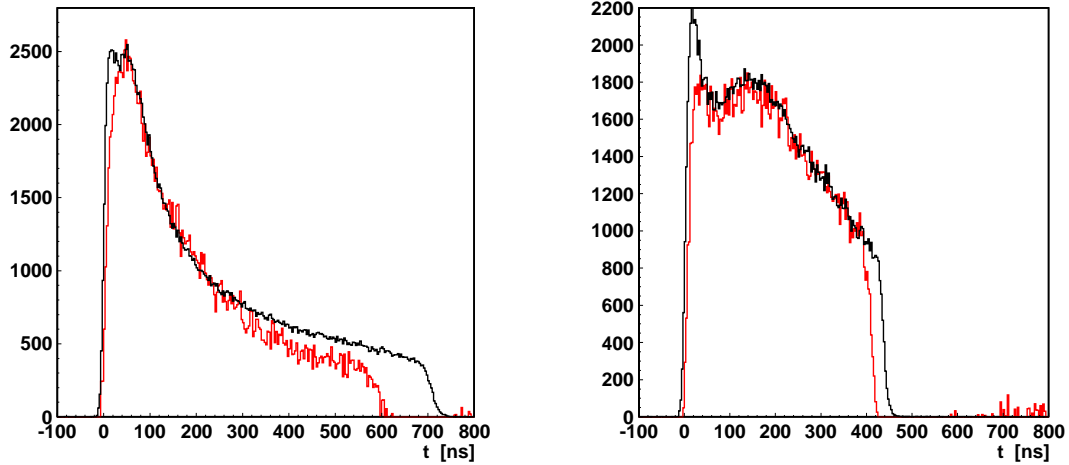
Figure 5.15: Drift time spectra measured in the GIF. The left plot shows the spectra in case of $Ar:CO_2$ $93:7$ without irradiation (black) and at an irradiation level of 1900 $\frac{Hz}{cm^2}$ (red). On the right plot the situation for the alternative gas mixture $Ar:CO_2:N_2$ $96:3:1$ is shown without (black) and with γ-irradiation (red).

is correlated to the amount of deviations. Looking at the drift time spectrum of the alternative gas mixture, the gain drop effect is also visible. But the maximum drift time decreases only by 40 ns. A broadening of the falling edge is almost not visible.

In view of the resolution degradation at big drift radii, the overlay of the experimentally determined rt-relations with (red) and without (black) γ-background in fig. 5.16 shows the radii, where space charge effects have influence on the drift properties. The effect due to background charges starts to be present at a radius of 7 mm for the standard gas and at 10 mm for the alternative gas mixture. One can also see that the effect is definitely smaller when using the N_2 gas mixture.

The drift time spectra as well as the rt - relations indicate, that the alternative gas mixture will provide a better resolution at high background rates. For the analysis of the resolution the upper- and lowermost multilayer (see fig. 5.17), which are shielded with lead bricks, are used to reconstruct the muon track. This track is extrapolated into the test multilayer, which is filled either with the standard or with the N_2 gas mixture.

The average resolution is given via the residual distributions. The width of the

68
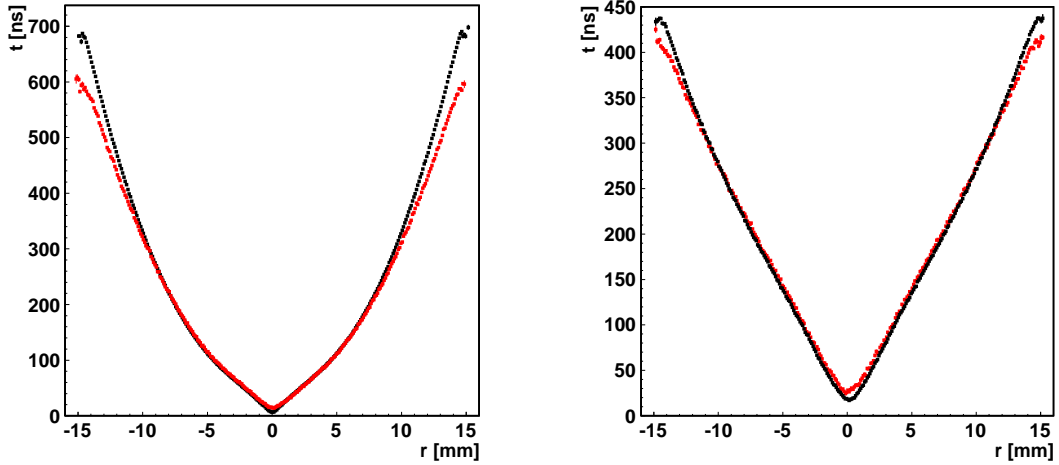
Figure 5.16: rt relation of standard gas (left) and the alternative gas mixture (right) in case of no irradiation (black) and an irradiation of 1900 $\frac{Hz}{cm^2}$ (red).

residual is 251 μm for $Ar:CO_2$ 93:7 without γ-background (fig. 5.18). At a background of 1900 $\frac{Hz}{cm^2}$ the resolution degrades by 92 μm to a value of 343 μm. Regarding the gas mixture $Ar:CO_2:N_2$ in a ratio of 96:3:1 the degradation is 31 μm from 255 μm (without background) to 286 μm (background) (fig. 5.19). The degradation in both cases is due to space charge fluctuations. The N_2 mixture shows better performance under high rates due to the fact that this gas mixture is more linear and therefore the drift velocity is less depending on the electric field variation.

The fact that the average resolution without background is about 250 μm in comparison to less than 100 μm has several reasons. The main contribution is due to the tracking uncertainty as only three tracking points above and three below the investigated multilayer contribute to the track fit. Furthermore the uncertainties due to multiple scattering and possible geometrical displacements overlaying the drill of the lower reference chamber, which can not be monitored, broaden the residual.
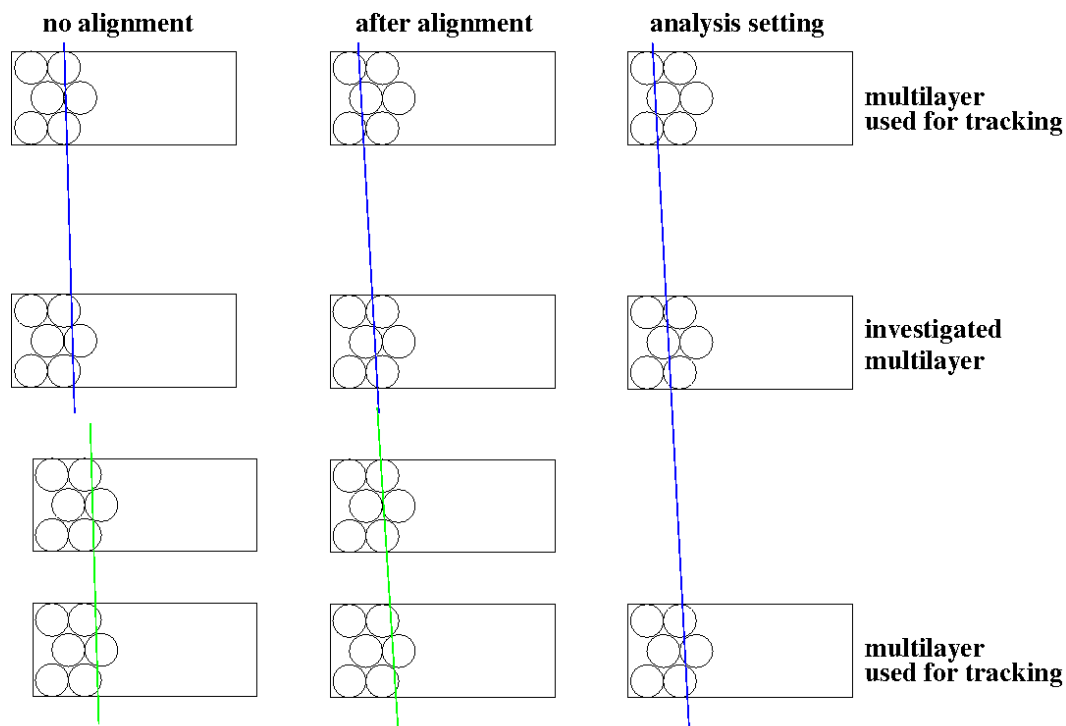
Figure 5.17: For the alignment two separately reconstructed tracks were used (left). The single tube resolution without background was determined using the setting in the middle, where the track of the upper chamber was used. The setting on the right was used for the high irradiation data, where only the lower- and uppermost multilayer were shielded and track reconstruction could be performed.

5.4 Summary

At the CRMF and in the GIF the resolution of the gas mixture $Ar : CO_2 : N_2$ in the ratio of $96 : 3 : 1$ was determined. It is similar to the resolution of the standard gas $Ar : CO_2$ in the ratio of $93 : 7$. The first measurement of the alternative gas mixture under high background rates showed less degradation of the resolution as the present ATLAS gas.
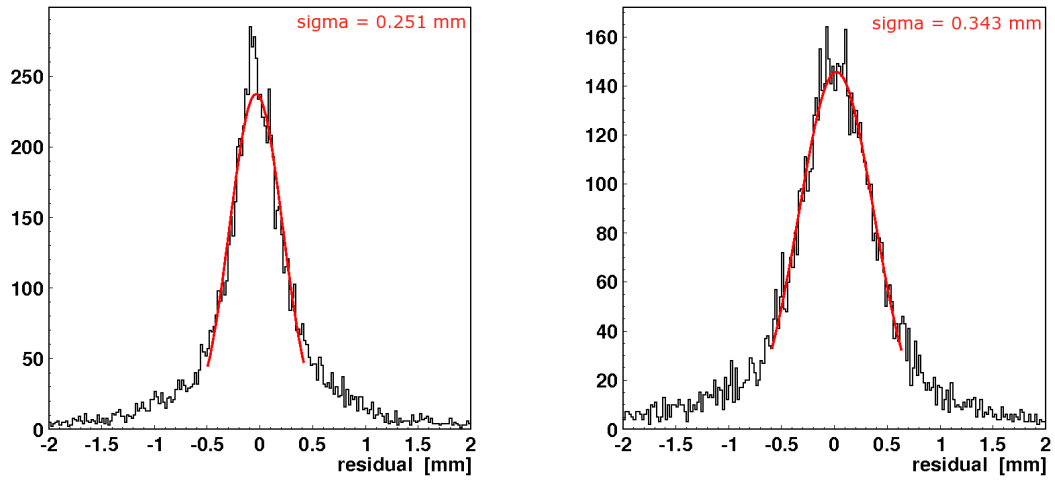
Figure 5.18: Width of residual in case of no γ-background (left) and with background (right).
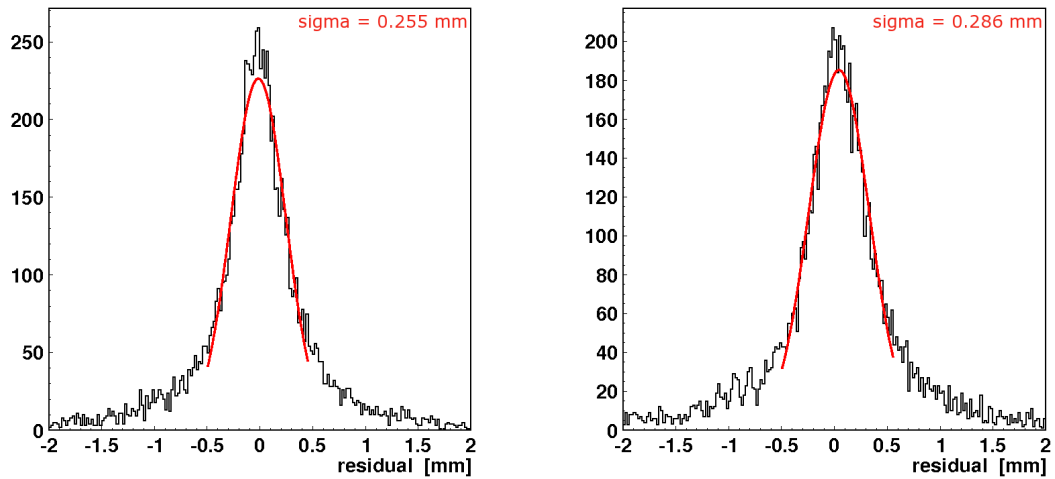
Figure 5.19: Width of residual in case of no γ-background (left) and with background (right).

71

6   DRIFT TUBES WITH A RADIUS OF 7.5 mm

In this chapter the results of the measurement period at the H8 facility at CERN are shown, where 15 mm drift tubes were tested for their resolution performance.

6.1   Principle

At higher background rates, the single tube resolution degrades due to space charge effects, especially for big radii (see fig 2.8 in chapter 2). Using 15 mm tubes [46, 47] instead of 30 mm and the same drift field, the maximum drift time is reduced from 700 to 180 ns (fig. 6.1). This means that the dead time of a tube is a quarter compared to the actual 30 mm tubes. Due to the reduction of the radius, the cross section of a tube for background hits is halved. Summing up
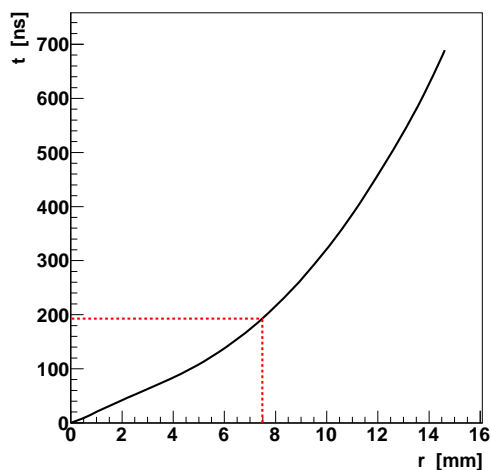
Figure 6.1: Rt-relation of Ar:CO2 93:7. Using tubes with r = 7.5 mm the maximum drift time is reduced to less than 200 ns and the rt-relation is more linear.

these two factors, the occupancy defined as

Eqn. 6.1: $$occupancy = hitrate \cdot t_{max}$$

of a tube in case of background hits is reduced by a factor of about 8. The other benefit of 15 mm tubes was stated in chapter 2. The gain drop and the field fluctuations due to space charges are smaller than for 30 mm tubes coming along with a smaller resolution degradation at high background rates. Furthermore t_{max}^{ion} is a quarter for 15 mm tubes compared to 30 mm tubes.
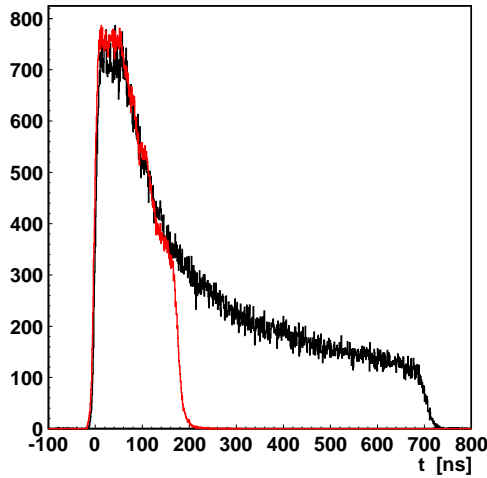
Figure 6.2: Drift time spectra of 30 mm (black) and 15 mm (red) tubes. The shapes of the spectra agree and the maximum drift time of 15 mm tubes is about four times shorter.

6.2 Performance at H8

The determination of the resolution of 15 mm drift tubes was performed at CERN using a beam of 140 GeV muons. The setup of the test beam is shown and explained in detail in chapter 3.3. It consists in principle of one 30 mm reference chamber and the 15 mm test chamber.

6.2.1 *Drift Time Spectra and Rt-Relation*

At identical electric field the shape of the drift time spectra is identical but the maximum drift time for 15 mm tubes is about 200 ns in comparison to 700 ns in

case of 30 mm tubes (see fig. 6.2).

6.2.2 *Muon Track Reconstruction*

A track is fitted, according to the scheme in chapter 4, separately to the measured radii of the 15 mm and 30 mm chambers. The results for the track parameters are shown in fig. 6.3 and 6.4. Looking at the y intercept, one observes distributions with a total width of about 50 mm in both chambers. This corresponds to the width of the scintillation counters used as muon trigger.

Furthermore there exist minima in the distributions due to less reconstructed tracks in certain regions. These can be identified as the wire and tube wall po-
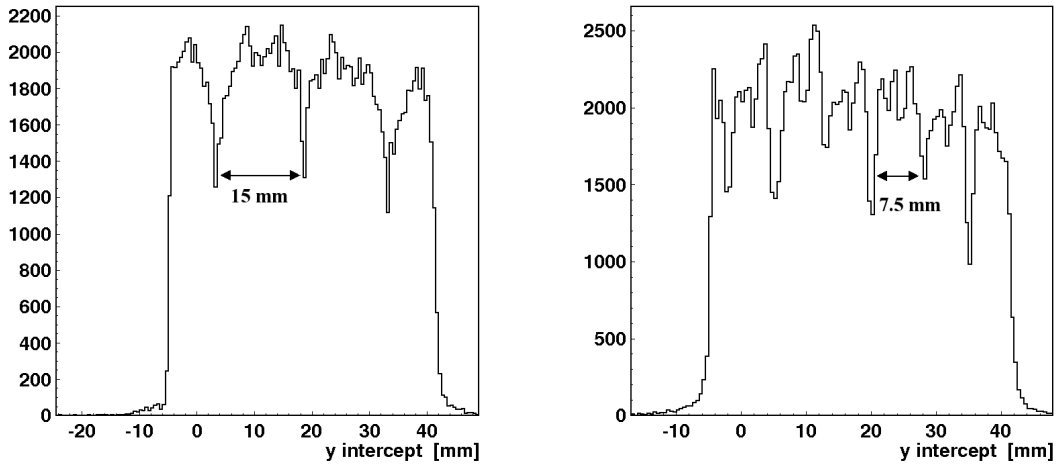
Figure 6.3: Y intercept distribution of the tracks reconstructed in the 30 mm (left) and 15 mm (right) chamber.

sitions in the first layer. The muon beam provided almost parallel tracks in z direction. Due to the assembling of the chambers, a muon, hitting a tube wall or wire in the first layer, will also hit a tube wall or wire in the other layers. In addition the distance between the minima are 7.5 mm and 15 mm in agreement with the radius of the tubes in the two chambers.

The slope distributions proof that all tracks are almost in parallel. The mean is 0.011 for both, but the width is very different. In case of the 30 mm chamber the width is $5 \cdot 10^{-4}$, whereas the 15 mm chambers width is $2 \cdot 10^{-3}$. Two effects account for this. The main effect is due to the fact, that the 30 mm chamber consists of two multilayers with a distance in between them of 320 mm compared to

74
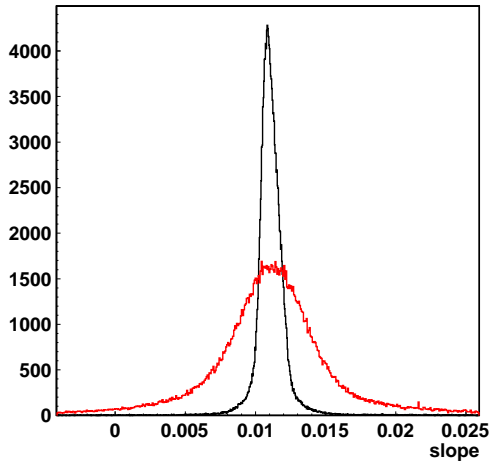
Figure 6.4: Slope distribution of the tracks reconstructed in the 30 mm (black) and 15 mm chamber (red).

one package of 8 layers of 15 mm tubes. Therefore one gets more precise tracking due to the lever arm [14]. The second thing is, that because of the trigger road almost all tracks hit the same tubes in the 30 mm chamber, whereas in the 15 mm chamber there are more possibilities. This causes also a degradation of the track reconstruction accuracy due to geometry, namely wire position and tube glueing tolerance.

The errors on the track parameters show on the first glance a dubious behaviour (fig. 6.5). One sees several maxima as well for the y intercept as for the slope error in both chambers. In case of the 30 mm chamber the second maximum is caused by tracks with 2 radii close to the wire. And the tail is due to tracks passing close to the wire in 4 tube layers.

In case of the 15 mm chamber 3 maxima occur. Looking at the y intercept distribution of tracks corresponding to these maxima, three regions can be extracted. In two regions there was a dead tube. Region 1, corresponding to the maximum at 490 μm for the y intercept, had a dead tube in layer 5 and region 3 (maximum at 685 μm) in layer 1. In these regions the track fit had 7 sampling points, whereas in region 2 the fit had 8 measured drift radii and the maximum is located at 627 μm. The broad tail corresponds like in case of the 30 mm chamber to tracks passing nearby the wire or tube wall.

The reason for the different errors in these three regions is due to the quasiana-
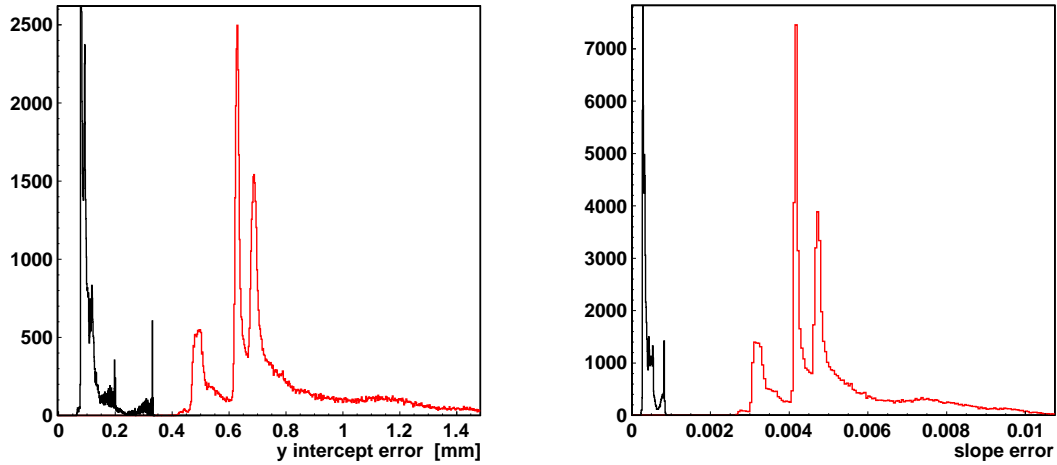
Figure 6.5: Errors on the track fit; left: y intercept, right: slope. The black distribution corresponds to the 30 mm tube chamber and the red one to the 15 mm tube chamber.

lytical track fit method [35], where combination of tube pairs, located in different multilayers, are used and the distance between the two regarded tube wires is critical. Without a tube in layer 5 combinations with minimal distance disappear and the fit is better as in case of the region with 8 hit tubes. Removing a tube in layer 1 worsens the fit accuracy due to the disappearance of combinations with a large lever arm. Calculations of the errors for these regions yields also three maxima at $512 \pm 31.7~\mu$m, $641 \pm 20.2~\mu$m and $706 \pm 35.4~\mu$m, which confirms the measurement.

6.2.3 Alignment

The reference chamber and the 15 mm chamber were only roughly aligned during the installation of the measurement setup. Comparing the slope and the y intercept of the tracks, which were reconstructed separately in the two chambers, the accurate alignment was performed. Due to the setup design and the fact that the tracks were almost parallel, only a precise correction for a y-shift and a rotation around x were possible.

The data showed a rotation of 21.7 mrad and a y-shift of 30 mm. After these
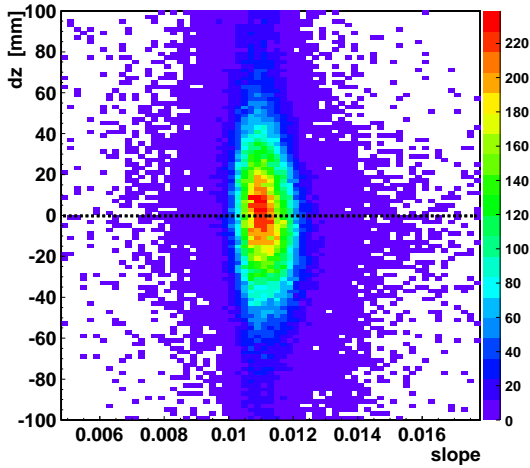
Figure 6.6: Distribution of dz versus slope. The difference in z was determined using the 15 mm chamber and the 30 mm chamber.

two corrections, the correlation between dz and slope is a broad distribution in a small slope range as shown in fig. 6.6. It is symmetric with respect to $dz = 0$, which indicates that the spacing between the 15 mm and the 30 mm is correct. The alignment accuracy is according to the distributions of the y intercept and the slope difference better than 10 μm in y direction and $3 \cdot 10^{-5}$ rad for the x rotation, according to fig. 6.7.

beam_20090825_2139_38mV_rot_0_0_INTERSECTDIFF_1	
Entries	172034
Mean	0.01422
RMS	0.7885
χ^2 / ndf	299.3 / 127
Constant	1535 ± 5.8
Mean	-0.005696 ± 0.001254
Sigma	0.3718 ± 0.0014

beam_20090825_2139_38mV_rot_0_0_SLOPEDIFF_1	
Entries	172034
Mean	-0.0001116
RMS	0.006164
χ^2 / ndf	338.8 / 102
Constant	2063 ± 7.6
Mean	$-2.304\mathrm{e}{-05} \pm 8.979\mathrm{e}{-06}$
Sigma	0.002815 ± 0.000010
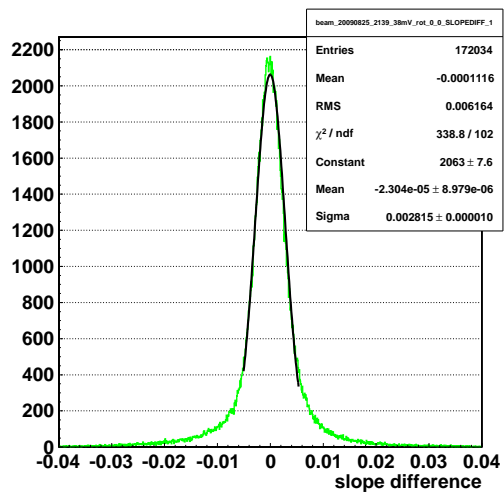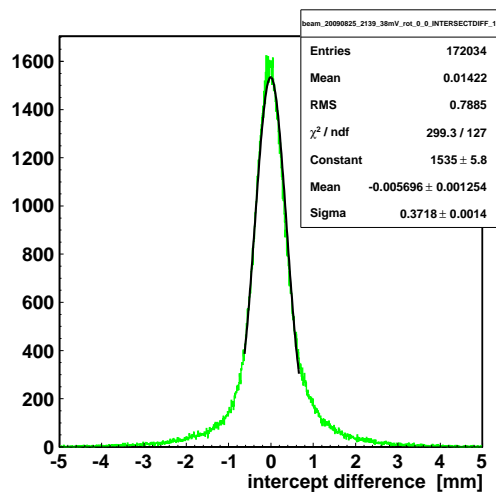
Figure 6.7: Intercept (left) and slope (right) difference after alignment.

6.2.4 *Resolution*

The determination of the resolution was performed as described in chapter 4 using tracks reconstructed with the 15 mm bundle and also via extrapolating the track from the reference chamber into the test chamber. Fifteen 15 mm tubes were fully irradiated and included in the analysis.

tube nr.	σ_{ref} $[\mu m]$	ϵ_{corr} $[\mu m]$	σ $[\mu m]$
5	186	163	89.6
10	182	160	86.7
11	183	160	88.8
16	181	157	90.1
17	178	157	83.9
22	179	153	92.9
23	180	153	94.8
28	174	150	88.2
29	178	150	95.8
34	177	147	98.6
35	175	147	95.0
40	170	143	91.9
41	163	143	78.2
46	175	140	105
47	175	140	105

Table 6.1: For all totally irradiated 15 mm tubes, the width of the residual σ_{ref}, the correction due to the track extrapolation ϵ_{corr} and the final single tube resolution of the 15 mm tubes is shown. Averageing over all tubes leads to a single tube resolution of 92.6 ± 6.98 μm.

Tab. 6.1 shows the measured width of residuals using the reference track σ_{ref}, the correction value derived from the track extrapolation ϵ_{corr} and the resulting single tube resolution given by

Eqn. 6.2:
$$\sigma = \sqrt{\sigma_{ref}^2 - \epsilon_{corr}^2} \; .$$

The extrapolation error consists of the error on the y intercept of 87.5 μm and the error on the slope of $3.1 \cdot 10^{-4}$, which is multiplied with the distance of the center

of gravity of the track in the reference chamber and the regarded tube wire in z direction. The z distance ranges from 354.5 mm for tubes 46 and 47 to 446.06 mm for tube 5. Taking all tubes into account, the average single tube resolution of the 15 mm tubes is 92.6 ± 6.98 μm.

The expectation from the analysis of 30 mm tubes is shown in fig. 6.8. The width of the residual of 30 mm tubes in the radius range of 0 to 7.1 mm is 91.2 μm, which is in agreement with the measured resolution of the 15 mm drift tubes. The determination of the resolution of 15 mm tubes, using reconstructed tracks in the chamber itself, yields to a value of 95 μm. It is slightly worse than the expectation from 30 mm tubes due to the fact that regarding a slice in 30 mm tubes does not account for close to wall effects, such as less produced charges in 15 mm tubes due to geometry.
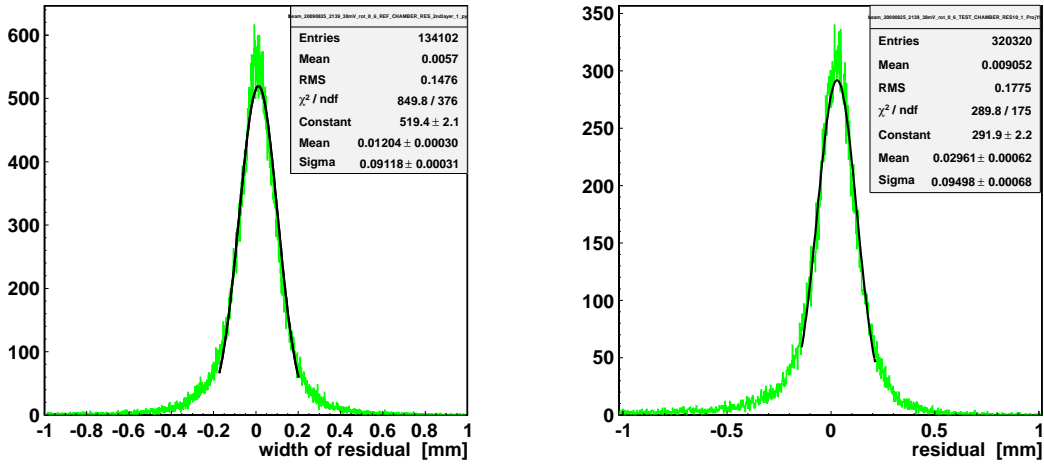
Figure 6.8: left: The width of the residual of 30 mm tubes for a radius slice from 0 to 7.1 mm is 91.2 μm, which is the expectation of the single tube resolution of 15 mm tubes. right: Residual of 15 mm drift tubes. The width is 95 μm.

The single tube resolution for the 30 mm and 15 mm tubes against the drift radius is shown in fig. 6.9. As expected, at small drift radii the resolution is in the order of 230 μm, improving to about 70 μm for big radii. The resolution of 15 mm tubes is similar to the one for 30 mm tubes up to radii of 7.1 mm. At small radii the resolution of 15 mm tubes is degraded because of low statistics and worsened track preciseness. This fact was explained above in context of the track fit errors. 2730 V gives the same drift field for 15 mm tubes as the ATLAS standard operation of 30 mm tubes. 2760 V raises the gas gain from 20000 to 25000 and therefore more

charges per muon are produced leading to a better resolution, which is visible as the black data points showing better resolution compared to the blue ones.
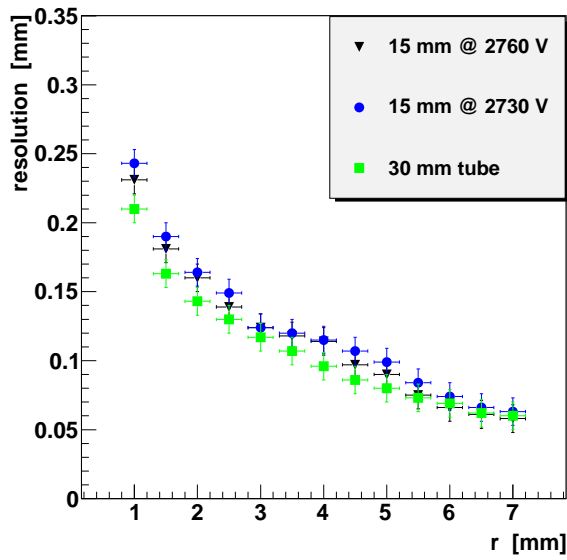
Figure 6.9: The resolution of 15 mm drift tubes for anode wire voltages of 2730 V and 2760 V and the expectation from 30 mm tubes are shown.

6.3   Summary

A bundle of 15 mm tubes was tested at the H8 facility at CERN. The resolution of 15 mm tubes agrees with the expectations derived from measurements with 30 mm tubes. The average resolution is better than 100 μm, which is the requirement on the tubes to achieve 10 % momentum resolution at an energy of 1 TeV.

7 SUMMARY AND OUTLOOK

The muon spectrometer of the ATLAS-experiment at the Large Hadron Collider consists of drift tube chambers, which provide the measurement of trajectories of trespassing muons. In order to determine the momentum of the muons with high precision in the toroidal magnetic field of ATLAS ($B \approx 0.5$ T), the measurement of the position of the muon in a single tube has to be more accurate than $\sigma \leq 100\,\mu$m.

The large cross section of proton-proton-collisions and the high luminosity of the accelerator cause relevant background in the muon spectrometer by neutrons and γs, which are produced in the shielding material and the detector components.

During the next decade a luminosity upgrade to $5 \cdot 10^{34}$ cm^{-2}s^{-1} is foreseen, which will also increase the background counting rates proportionally. Under high background conditions the present muon chambers show a critical resolution degradation and a high occupancy of the drift tubes due to the non-linearity and the maximum drift time of 700 ns of the drift gas. Therefore parts of the so-called Small Wheel have to be replaced by detectors with higher rate capability. For the rest of the spectrometer dealing with lower counting rates an alternative gas mixture can provide sufficient position measurement accuracy without replacing the existing hardware components.

Regarding fastness, linearity, afterpulsing, streamer rate and inertness of gas components, the gas mixture $Ar : CO_2 : N_2$ in the ratio of $96 : 3 : 1$ Vol % is a valuable candidate to replace the present gas mixture $Ar : CO_2$ in the ratio of $97 : 3$ Vol %. This alternative gas is with a maximum drift time of 450 ns 35 % faster and by far more linear than the ATLAS gas. Therefore the drift tubes are less occupied and the electron drift in the gas is less influenced due to space charges. The resolution of this alternative gas was determined at the CRMF and in the GIF without background. It is similar to the resolution of the standard gas, ranging between 230 μm for small radii and 70 μm for big radii. Both measurements agree with each other.

The use of drift tubes with halved radius, using the standard gas under the same operation parameters, at a high voltage of 2730 V, which was adapted to create

the same electric field as for 30 mm tubes, reduces the maximum drift time by a factor 4 to a value of 180 ns. The reduction of the radius further yields to halved cross section of the tube to background. The occupancy is therefore reduced by a factor 8. Furthermore the space-time relation is almost linear causing only a small degradation of the resolution due to space charges. 15 mm drift tube detectors are therefore reasonable candidates for precise and efficient muon track reconstruction in high rate environments. A 15 mm drift tube chamber was operated at the H8 test facility at CERN, where a muon beam provided muons with an energy of 140 GeV. The single tube resolution of 15 mm tubes was determined to be 95 μm in agreement with expectations from 30 mm tubes.

At both experiments reference chambers for exact muon track reconstruction were included in the experimental setups. To determine resolutions below 100 μm with an external reference, the setup components have to be aligned very precisely. It was a main effort of this thesis to develop a method to correct for incomplete alignment or geometrical deviations from nominal settings. For the H8 test beam measurement a 2 dimensional correction had to be applied as the beam muons were parallel and the trigger surface was only 25 cm^2. The setup in the GIF was reconstructed 3 dimensional by using the residual distributions produced via reference tracks and the comparison of the track parameters along the anode wires. The lower reference chamber in this setup was drilled along x. The alignment accuracy in y was smaller than 10 μm, smaller than 30 μm in z and for the rotation around x smaller than $4 \cdot 10^{-5}$ rad for the GIF setup as well as for the H8 setup, given by the mean values of the distributions for the slope difference and the intercept difference. The width of the difference distributions of slope and intercept are hereby only $2 \cdot 10^{-3}$ and 260 μm, respectively.

After these geometrical corrections the resolution of the standard gas and the alternative gas was determined at a γ-background counting rate of 1900 $\frac{\text{Hz}}{\text{cm}^2}$. For the ATLAS gas the resolution degraded by 92 μm, which is in agreement with an earlier measurement. But the alternative gas showed a resolution degradation of only 31 μm at this background rate.

In the present work I could show that single tube resolutions below 100 μm are achievable using 30 mm and 15 mm drift tube technology. Alignment tools allow for geometrical corrections of the setup with an accuracy of 30 μm in position and $4 \cdot 10^{-5}$ in slope (= 40 μm per m distance). The resulting width of the difference distributions between slope and intercept in the reference chamber and the chamber to be investigated demonstrate that the experimental setup used for the GIF and the H8 experiments were insufficient. The used reference chamber at

H8 reached only tracking accuracies around 160 μm. The setups were designed in collaboration with the Max-Planck-Institut für Physik dealing with boundary conditions, e.g. the GIF source's geometry and, for the H8 measurement, the not properly operating silicon telescope.

An optimised setup would use reference tracking systems with longer lever arm, more precise determination of the track parameters, enclosing the detector to be investigated, e.g. in case of drift tube detectors 6 tracking points on each side of the investigated object.

LIST OF FIGURES

BIBLIOGRAPHY

[1] **Scandale, W. and Zimmermann, F.:**
Final CARE-HHH Workshop on Scenarios for the LHC Upgarde and FAIR.
CERN-2009-004; CARE-Conf-08-032-HHH, CERN 2009

[2] **Brüning, O. (ed.) et al.:**
LHC design report. Vol. I: The LHC main ring.
CERN-2004-003-V-1, CERN 2004

[3] **Atlas Collaboration, Aad, G. et al.:**
The ATLAS Experiment at the CERN Large Hadron Collider.
JINST 3 S08003, 2008

[4] **Della Negra, M. et al.:**
CMS physics: Technical Design Report, v.1: Detector performance and software.
CERN-LHCC-2006-001, CERN 2006

[5] **LHCb Collaboration:**
LHCb reoptimized detector design and performance: Technical Design Report.
CERN-LHCC-2003-030, CERN 2003

[6] **Cortese, P. et al.:**
ALICE physics performance: Technical Design Report.
CERN-LHCC-2005-030, CERN 2005

[7] **Caron, J.-L.:**
The LHC injection complex.
LHC-PHO-1993-008, CERN 1993

[8] **ATLAS-WIKI:**
https://twiki.cern.ch/twiki/bin/view/AtlasPublic/AtlasTechnicalPaperListOfFigures
URL last visited: June 2011

[9] **Atlas Collaboration:**
Atlas Inner Detector Technical Design Report.
CERN-LHCC-97-16 and 97-17, CERN 1997

[10] **Atlas Collaboration:**
Atlas Calorimeter Performance Technical Design Report.
CERN-LHCC-96-40, CERN 1996

[11] **Atlas Collaboration:**
Atlas Muon Spectrometer Technical Design Report.
CERN-LHCC-97-022, CERN 1997

[12] **Grupen, C.:**
Teilchendetektoren.
B.I. Wissenschaftsverlag, 1993

[13] **Charpak, G.:**
Annual Review of Nuclear Science 20.
Annual Reviews Inc., 1970

[14] **Kleinknecht, K.:**
Detektoren für Teilchenstrahlung.
Teubner Studienbücher, 1992

[15] **Leo, W.R.:**
Techniques for Nuclear and Particle Physics Experiments.
Springer Verlag, New York 1994

[16] **Engl, A.:**
Temperaturstudien an ATLAS-MDT-Myondetektoren.
Diploma thesis, LMU Munich 2007

[17] **van der Graaf, H.:**
Alignment System for the ATLAS MDT Barrel Muon Chambers - Technical System Description.
NIKHEF/ET38110, 2000

[18] **Arai, Y. et al.:**
AMT-3 User's Manual.
KEK, Japan 2003

[19] **Posch, C., Hazen, E., Oliver, J.:**
MDT-ASD User's Manual.
ATL-MUON-2002-003, CERN 2002

[20] **Arai, Y. et al.:**
ATLAS Muon Drift Tube Electronics.
JINST 3 P09001, 2008

[21] **Baranov, S.:**
Estimation of Radiation Background, Impact on Detectors, Activation and Shielding Optimization in ATLAS.
ATL-GEN-2005-001, CERN 2005

[22] **Jeanty, L.:**
Cavern Background in the Muon System.
Talk at the Muon Upgrade Meeting, CERN April 12th 2011

[23] **Aleksa, M. et al.:**
MDT Performance in a High Rate Background Environment.
ATL-MUON-98-258, CERN 1998

[24] **Riegler, W.:**
Limits to Drift Chamber Resolution.
Doctoral Thesis, TU Vienna 1997

[25] **Scherberger, G. et al.:**
High Rate Performance of MDTs.
ATL-MUON-NO-177, CERN 1997

[26] **Horvat, S. et al.:**
Operation of ATLAS muon drift-tube chambers at high background rates and in magnetic fields.
IEEE Trans. Nucl. Sci. 53 no. 2 (562-566), 2006

[27] **Diethorn, W.:**
A methane proportional counter system for natural radiocarbon measurements.
USAEC Report NY06628, 1956

[28] **Aleksa, M., Riegler, W.:**
Non-Linear MDT Drift Gases like Ar/CO2.
ATL-MUON-98-268, CERN 1998

[29] **Rauscher, F.:**
Untersuchung des Verhaltens von Driftrohren bei starker γ Bestrahlung sowie Vermessung von Driftrohrkammern mit Hilfe von Myonen der kosmischen Höhenstrahlung.
Doctoral thesis, Munich 2005

[30] **Biebel, O. et al.:**
A Cosmic Ray Measurement Facility for ATLAS Muon Chambers.
LMU-ETP-2003-01, Munich 2003

[31] **Berberis, J. et al.:**
High-precision X-ray tomograph for quality control of the ATLAS muon monitored drift chamber.
Nucl. Instrum. Methods Phys. Res. A 419 (342-350), 1998

[32] **CERN:**
http://nahandbook.web.cern.ch/
URL last visited: June 2011

[33] **Efthymiopoulos, I. and Fabich, A.:**
The Very Low 1-9 GeV/c Tertiary Beam Extension of the H8 beam Line of CERN SPS.
CERN-AB-2005-036, CERN 2005

[34] **Kortner, O. and Rauscher, F.:**
Automatic Synchronization of Drift-Time Spectra and Maximum Drift-Time Measurement of an MDT.
ATL-COM-MUON-2002-006, CERN 2002

[35] **Kortner, O.:**
Schauerproduktion durch hochenergetische Myonen und Aufbau eines Höhenstrahlungsprüfstandes für hochauflösende ATLAS-Myonkammern.
Doctoral Thesis, LMU Munich 2002

[36] **Rauscher, F.:**
Test von Driftkammern mit kosmischen Myonen: Bau der ersten Ausbaustufe des Teleskops und Untersuchung seiner Leistungsfähigkeit.
Diploma thesis, LMU Munich 2001

[37] **Adomeit, S.:**
Konstruktion, Bau und Einsatz eines Szintillator-Trigger-Hodoskops.
Diploma Thesis, LMU Munich 2010

[38] **Cirilli, M. et al.:**
Results from the 2003 beam test of a MDT BIL chamber: systematic uncertainties on the TDC spectrum parameters and on the space-time relation.
ATL-MUON-2004-028, CERN 2004

[39] **Bagnaia, P. et al.:**
Calib: a package for MDT calibration studies - User Manual.
ATL-MUON-2005-013, CERN 2005

[40] **Mlynek, A.:**
Ortsauflösung der Driftrohre des ATLAS-Myonspektrometers bei Neutrone-nuntergrund.
Diploma thesis, LMU Munich 2006

[41] **Lang, P.:**
Studien zur Gasmischung an MDT-MYON-Detektoren.
Diploma thesis, LMU Munich 2008

[42] **Tyler, N.:**
Analyse der Pulsform und Untergrundeigenschaften von Ar-CO2-N2 Drift-gasen an MDT-Driftrohren.
Master thesis, LMU Munich 2011 (in preparation)

[43] **Scherberger, G.:**
Aufbau und Test von Hochdruck-Driftröhren.
Diploma thesis, Uni Freiburg 1994

[44] **LUMA Metall AB:**
Product sheet of Gold plated Tungsten-Rhenium Wire: http://www.luma-metall.se/
URL last visited, June 2011

[45] **Engl, A. et al.:**
ATLAS monitored drift tube chambers for super-LHC.
Nucl. Instrum. Methods Phys. Res. A 623 (91-93), 2010

[46] **Bittner, B., ... Engl, A., ... et al.:**
Development of Muon Drift-Tube Detectors for High-Luminosity Upgrades of the Large Hadron Collider.
Nucl. Instrum. Methods Phys. Res. A 617 (169-172), 2010

[47] **Bittner, B., ... Engl, A., ... et al.:**
Development of Fast High-Resolution Muon Drift-Tube Detectors for High Counting Rates.
Nucl. Instrum. Methods Phys. Res. A 628 (154-157), 2011

DANKSAGUNG

Mein herzlicher Dank gebührt an erster Stelle Prof. Otmar Biebel, der mir in jeder Phase meiner Arbeit als Doktorvater mit Rat und Tat zur Seite stand. Darüberhinaus danke ich ihm auch als Sprecher des Graduiertenkollegs „Teilchenphysik im Energiebereich neuer Phänomene", das von der DFG gefördert wird und mir durch ein Stipendium die finazielle Unterstützung für mein Doktorvorhaben gegeben hat.

Desweiteren danke ich Herrn Dr. Ralf Hertenberger für die exzellente Betreuung und viele hilfreiche Ideen.

Ich danke Herrn Prof. Wolfgang Dünnweber für die Erstellung des Zweitgutachtens.

Frau Prof. Dorothee Schaile danke ich für die herzliche Aufnahme an Ihrem Institut.

Frau Herta Franz danke ich für die zuverlässige Unterstützung bei bürokratischen Angelegenheiten.

Für das Korrekturlesen dieser Arbeit möchte ich mich bei Alexander Ruschke, Nicola Tyler, Dr. Ralf Hertenberger und Prof. Otmar Biebel bedanken.

Die Arbeitsatmosphäre hier am Lehrstuhl war hervorragend. Dafür danke ich allen Mitgliedern recht herzlich.
Einen besonderen Dank möchte ich David Heeremann, Jonathan Bordtfeld, Alexander Ruschke, Stefanie Adomeit und Andre Zibell aussprechen für die unzähligen gemeinsamen erheiternden Kaffeepausen.

Mein weiterer Dank gilt Bernhard Bittner, Federica Legger und Felix Rauscher für den Input in Sachen MT-Offline und die tolle Atmosphäre während diverser Messperioden am CERN.

Zuletzt danke ich meiner Familie für die Unterstützung während meines Studiums und der Doktorarbeit.

Meiner Verlobten Caro und meiner Tochter Marie danke ich, dass Sie mir immer den Rücken gestärkt haben und vor allem gegen Ende meiner Arbeit mir jeden Abend mit einem Lächeln neue Kraft gegeben haben.